DOI:10.14753/SE.2024.3055

SEMMELWEIS EGYETEM

DOKTORI ISKOLA

Ph.D. értekezések

3055.

SZÖLLŐSI DÁVID

Celluláris és molekuláris biofizika

című program

Programvezető: Dr. Kellermayer Miklós, egyetemi tanár

Témavezető: Dr. Szigeti Krisztián, tudományos főmunkatárs

DOI:10.14753/SE.2024.3055

IN VIVO IMAGING METHODS FOR STUDYING HOST-MICROBIOTA INTERACTIONS

PhD thesis

Dr. Dávid Szöllősi

Doctoral School of Theoretical and Translational Medicine

Semmelweis University

Supervisor: Krisztián Szigeti PhD

Official reviewers:

Bóta Attila PhD, DSc

Pállinger Éva PhD

Head of the Complex Examination Committee:

Varga Gábor PhD, DSc

Members of the Complex Examination Committee:

Ambrus Csaba PhD

Vásárhelyi Barna PhD, DSc

Budapest

2024

DOI:10.14753/SE.2024.3055

Table of Contents

DOI:10.14753/SE.2024.3055

DOI:10.14753/SE.2024.3055

List of Abbreviations

Abbreviation	Meaning
AIDA-I	adhesin involved in diffuse adherence
AMPA	α-amino-3-hydroxy-5-methylisoxazole-4-propionic acid
ATR-FTIR	attenuated total reflectance Fourier-transform infrared spectroscopy
BSA	bovine serum albumin
CLINME	6-chloro-2-(4′-iodophenyl)-3-(N,N-methylethyl)imidazo[1,2-a]pyridine-3-acetamide
CT	computed tomography
EDTA	Ethylenediaminetetraacetic acid
EMG	exponentially modified Gaussian
EV	extracellular vesicle
FCM	flow cytometry
FRT	flippase recognition target
FWHM	full width at half maximum
GEMG	general exponentially modified Gaussian
GRE	gradient recalled echo
Hbp	haemoglobin binding protease
H:gm	Salmonella enterica serovar Enteritidis flagellar protein
HPLC	high performance liquid chromatography
IPTG	isopropyl β-d-1-thiogalactopyranoside
LB	lysogeny broth
LPS	lipopolysaccharide
MD-2	myeloid differentiation factor 2
MRI	magnetic resonance imaging
NODAGA	1-(1,3-carboxypropyl)-4,7-carboxymethyl-1,4,7-triazacyclononane
OM	outer membrane vesicle
OMV	outer membrane vesicle
PBR	peripheral benzodiazepine receptor
PBS	phosphate buffered saline
PCR	polymerase chain reaction
PET	positron emission tomography
RCP	radiochemical purity
SAE	sepsis associated encephalopathy
SDS-PAGE	sodium dodecyl sulfate-polyacrylaminde gel electrophoresis
SEC	size exclusion chromatography
SefA	Salmonella enterica serovar Enteritidis fimbrial protein
SpC	SpyCatcher
SPECT	single photon emission computed tomography

SpT	SpyTag
SpT-CF	SpyTag-carboxyfluorescein
SUV_{mean}	mean standardized uptake value
TEM	transmission electron microscopy
TLR-4	toll-like receptor 4
TSPO	18 kDA translocator protein
VOI	volume of interest

DOI:10.14753/SE.2024.3055

1. Introduction

We have a vital relationship with our microbiota that affect our lives in ways that we only start to understand. Bacteria are the most abundant members in our microbiome comprising a variety of commensal, mutualistic and pathogenic strains. Their composition and function facilitates our development throughout life and can mean the difference between health and disease. There are a variety of important bacterial mediators that can elicit local or systemic responses from the host and insight into their functions drives the development of novel diagnostic and therapeutic approaches in medicine today.

The glycolipid lipopolysaccharide (LPS) -also called endotoxin- is the main component of the outer leaflet of the outer membrane (OM) of Gram negative bacteria. It is composed of three structural domains: i) the O antigen which is a highly variable polysaccharide made of repeating oligosaccharides, ii) the core oligosaccharide which usually contains 3-deoxy-D-manno-oct-2-ulosonic acid, heptoses and hexoses, sometimes modified with different substituents, and iii) lipid A which is an acylated glucosamine disaccharide modified with phosphate groups. LPS has high immunogenicity mostly due to the lipid A component (1). In the host, LPS/lipid A is recognized by the toll-like receptor 4/myeloid differentiation factor 2 (TLR-4/MD-2) complex expressed on the surface of phagocytes. Recognition by this receptor complex results in the expression of pro-inflammatory cytokines serving as the main driving forces in early sepsis. Importantly, the structure of lipid A can highly influence the LPS/TLR-4 interaction. The number, position and length of acyl groups, and the number of phosphate groups determines the immunogenic potential of lipid A (2). It has been shown that penta-acylated lipid A produced by LpxM knockout strains has a markedly lower immunogenic potential compared to hexa-acylated LPS, which is normally produced by most Gram-negative strains (3-6). Another important recognition pathway which is followed by intracellular delivery of LPS is initiated by caspase 11 (in mice) or caspase 4 and 5 (in humans) and leads to pyroptosis of the affected cell. Notably, intracellular LPS delivery can be facilitated by outer membrane vesicles (OMVs) (2).

The systemic effects of LPS can vary from devastating septic shock to chronic inflammation. Different levels of organ dysfunction is associated to all levels of this

spectrum. An important target organ of systemic inflammation is the brain, where it can elicit the activation of the innate immune system leading to neuroinflammation. Sepsis associated encephalopathy (SAE) is a neuroinflammatory disease caused by sepsis. It is associated with both acute and long-lasting neurological dysfunction and contributes to the mortality of patients with sepsis (7). An important animal model of SAE is the LPS-induced murine systemic inflammation model. In this model, endotoxemia following the systemic administration of LPS causes the global activation of immune system leading to cytokine and chemokine storm. These inflammatory mediators and LPS cause neuroinflammation in the brain characterized by elevated cytokine levels (8-13), microglia activation (13, 14), neuron damage (8), altered neurotransmission (15), oxidative stress (8, 16), blood-brain barrier changes (8, 17) and vascular adhesion (18) or invasion (19) of immune cells. Studying the dynamic nature and regional specifics of these processes could lead to a better understanding of pathophysiology and may lead to novel therapeutic approaches aimed at protecting the brain in sepsis. In vivo nuclear medicine imaging can be used to achieve this goal.

Microglia activation plays a central role in neuroinflammation (20). Microglia are the resident immune cells in the brain. They have a wide variety of functions, including defense against invading pathogens, cleaning up cellular debris and amyloid deposits, regulating neuronal activity and blood flow (21, 22). During neuroinflammation their “resting” phenotype quickly changes to an “active” phenotype. These terms are now regarded as misnomers as these cells are never truly resting, and their activation leads to many distinct phenotypes, some of which are pro-inflammatory, while others are anti-inflammatory, serving as regulators of the immune response (23). Due to the important roles of microglia in neurodegenerative diseases and stroke, there is an ongoing effort to develop methods to detect their activation using molecular imaging. The most thoroughly investigated imaging target is the 18 kDa translocator protein (TSPO), formerly known as peripheral benzodiazepine receptor (PBR). Early experiments indicated that this molecule is localized on the outer membrane of mitochondria where it plays an essential role in steroid synthesis as a translocator. For decades it was generally accepted that in the brain, TSPO is expressed in astrocytes and microglia and during neuroinflammation, its expression is increased in correlation with microglia activation. Recent evidences that emerged in the 2010’s and

2020's however contradict our previous beliefs and mechanistic views. Experiments with the first TSPO knockout mouse strain suggested that it doesn't play an essential role in steroidogenesis and TSPO knockouts live to a full lifespan with no noticeable growth of behavioral differences (24). It was also shown that TSPO is expressed in the cytoplasm, the perinuclear region, and the cell membrane, and its overall expression in the brain is not so strongly tied to microglia only, as neurons, endothelial cells and invading peripheral macrophages also express the protein (25, 26). Furthermore, recent results suggest that TSPO upregulation during microglia activation is a trait specific to the *Muroidea* superfamily of rodents (including mice and rats), therefore, in human subjects the increase of TSPO tracers in neuroinflammation most likely corresponds with microglia density rather than activation state (27, 28). In light of all this new information, the results of preclinical and clinical molecular imaging studies, dating back to the 1980's should be reinterpreted (25).

There are a wide variety of TSPO tracers available in the literature with different chemical properties and pharmacokinetics (29). The tracer 6-chloro-2-(4′-iodophenyl)-3-(N,N-methylethyl)imidazo[1,2-a]pyridine-3-acetamide (CLINME), was originally designed for ^{11}C radiolabeling. [^{11}C]CLINME outperformed [^{11}C]PK11195 (the gold standard first generation TSPO tracer) in positron emission tomography (PET) imaging signal-to-background ratio (30). It was later shown that SPECT imaging with [^{123}I]CLINME produces similar results in the rat model of unilateral excitotoxic brain lesion elicited by the unilateral striatal injection of α-amino-3-hydroxy-5-methylisoxazole-4-propionic acid (AMPA) (31). The uptake of [^{123}I]CLINME spatially correlated with the site of the lesion, which was characterized by neuron loss, microglial activation, and astrocyte activation to a lesser extent. In this model, the activation of AMPA receptors causes the influx of sodium and calcium ions into the neurons causing cellular dysfunction and ultimately cell death followed by microglial response resulting in localized neuroinflammation.

Iodine labeling has some very important benefits compared to ^{11}C. First of all, iodine is more versatile having many useful isotopes such as ^{123}I for SPECT imaging, ^{124}I for PET imaging, ^{125}I for single photon emission computed tomography (SPECT) imaging and ex vivo studies and ^{131}I for radiotherapy and SPECT imaging. Furthermore, the biggest challenge in ^{11}C radiochemistry is its 20.3-minute half-life, which creates significant

infrastructural requirements (e.g. distance from cyclotron facility) and labs working with this isotope generally have to be equipped with specific tools to be able to carry out very fast synthesis while handling highly radioactive samples. On the other hand, iodine isotopes generally have more favorable half-lives making handling and radiochemical procedures less demanding. Although there had been multiple PET studies to investigate the neuroinflammatory effects of endotoxemia (32-34), CLINME SPECT imaging had not been evaluated prior to our work.

Endotoxemia is just one possible consequence of living with bacteria. There are many other mediators to consider in host-microbiota interactions (35). Among these mediators, OMVs produced by Gram negative bacteria are especially interesting due to their complexity and functional diversity (36). OMVs are nano-sized extracellular vesicles (EVs) released by Gram-negative bacteria into their environment (Fig. 1.).

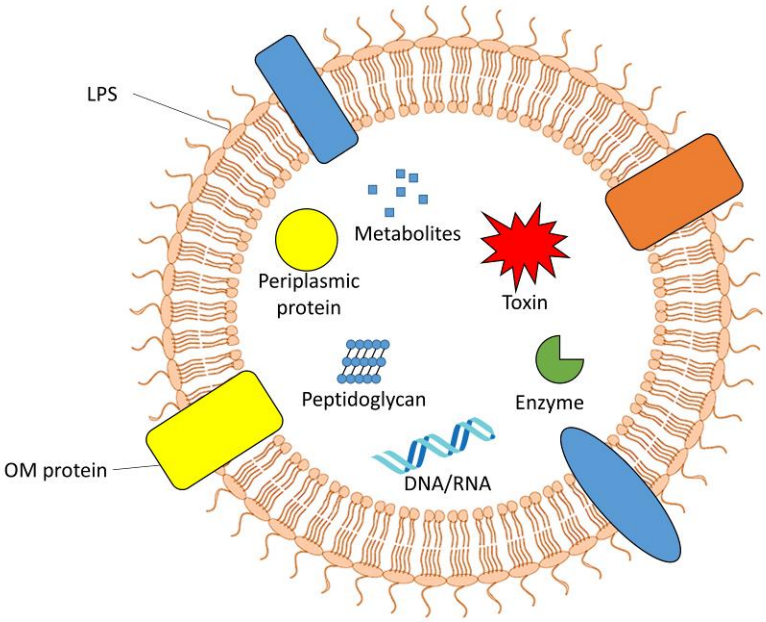

Fig. 1. ***The structure and composition of OMVs.*** *Due to their origin, OMVs contain outer membrane components (LPS, phospholipids, OM proteins) and may also contain various periplasmatic components such as metabolites, toxins, peptidoglycan fragments, enzymes and other proteins, DNA and/or RNA.*

DOI:10.14753/SE.2024.3055

OMVs are released from the OM by budding and membrane fission, although the exact mechanisms involved in their biogenesis are not fully understood (37). Their protein and lipid composition strongly resemble that of the OM and the periplasmic space, however, some significant differences suggest the possibility that sorting mechanisms are involved in their formation (37, 38). Their roles in the life of bacteria and participation in host-microbiota interactions are diverse, taking part in bacterial competition, biofilm formation, gene transfer, nutrient transport, antibiotic resistance, and stress response mechanisms while also serving as virulence factors (38-40). Their contribution to the host's immune homeostasis and their role in many diseases and disorders have also been demonstrated recently (40) making them prime candidates for diagnostics and even therapy.

Outer membrane vesicles are also emerging as a versatile vaccine platform due to their excellent adjuvant properties and ease of modification by genetic engineering, allowing researchers to express a wide array of foreign antigens on their surface (41, 42). Genetically engineered OMVs are a promising platform for targeted drug delivery applications, as demonstrated by their inherent tumor-targeting capabilities (43) and the possibility of introducing specific targeting molecules on their surface to increase this targeting efficiency (4). Their lumen can also be loaded with therapeutic compounds (5).

Despite ongoing research interest in OMVs and their prospects in the pharmaceutical industry, our knowledge regarding their biodistribution is limited. Reports of their distribution have only been published in healthy animals and selected disease models (5, 44-48). It would be exciting to see how specific strain-based differences, mutations, or host pathologies affect the biodistribution of OMVs, however, quantifying their biodistribution is challenging. The most widely used methods are based on fluorescent labeling and measuring with either whole-body fluorescence imaging devices or microscopy. Although the organs of the animals can be harvested at different time points and imaged separately, it is apparent that these methods do not allow easy and precise quantification of biodistribution on the scale of organs or the whole animal, especially if one wishes to determine pharmacokinetic parameters. There have been some advances to address these challenges, including methods for optoacoustic imaging (49) and radiolabeling methods (50-52).

Nuclear medicine imaging may offer a solution to these challenges. Advances in imaging methods allow the in vivo robust quantification of radiolabeled compound tissue concentrations at multiple time points in the same animal in 3D. The key to these methods is to use a radiolabeling procedure that can enable the detection of the compound of interest, in this case, OMVs. In theory, there are many possible ways to approach OMV radiolabeling with different benefits and limitations. To our knowledge, OMV radiolabeling for in vivo imaging has only been reported three times in the literature. Pastor et al. presented a radiolabeling method (50) based on the classic stannous-chloride reduction of technetium. Siddiqui et al. (51) describe a method for the radiolabeling of bacteria and OMVs for PET based on the bacterial expression of FyuA, an outer membrane receptor for the metallophore yersiniabactin. They demonstrated that ^{64}Cu-labeled yersiniabactin can be incorporated into FyuA-expressing bacteria and their OMVs selectively. Zhe Li et al. (52) report a deferoxamine-based ^{89}Zr-labeling method of avian pathogenic *E. coli* OMVs.

There are multiple OMV components that could serve as targets for a radiolabeling method. A relatively new approach in EV imaging is the use of genetic engineering to modify the source organism so that it produces a protein which facilitates specific and efficient EV radiolabeling (53). Surface display is a bioengineering technique usually used to anchor polypeptides to the bacterial outer membrane for various purposes, and in theory, could be used to decorate the OMV surface with molecules that facilitate radiolabeling. It is usually achieved by inserting the desired polypeptide chain into an extracellular region of an outer membrane protein. One such group of membrane proteins that can be used for this purpose is autotransporters. Autotransporters are part of the type V secretion system (54, 55). The best-known and most widely researched subgroup is the type Va group, also known as classical autotransporters. Having a monomeric structure, they consist of three main regions: i) an N-terminal signal sequence, responsible for Sec-dependent transport across the inner membrane, ii) a passenger domain that determines the functional traits of the autotransporter and iii) a C-terminal translocation unit that integrates into the OM allowing the translocation of the passenger domain through the membrane (56). An example is illustrated in Fig. 2.

DOI:10.14753/SE.2024.3055

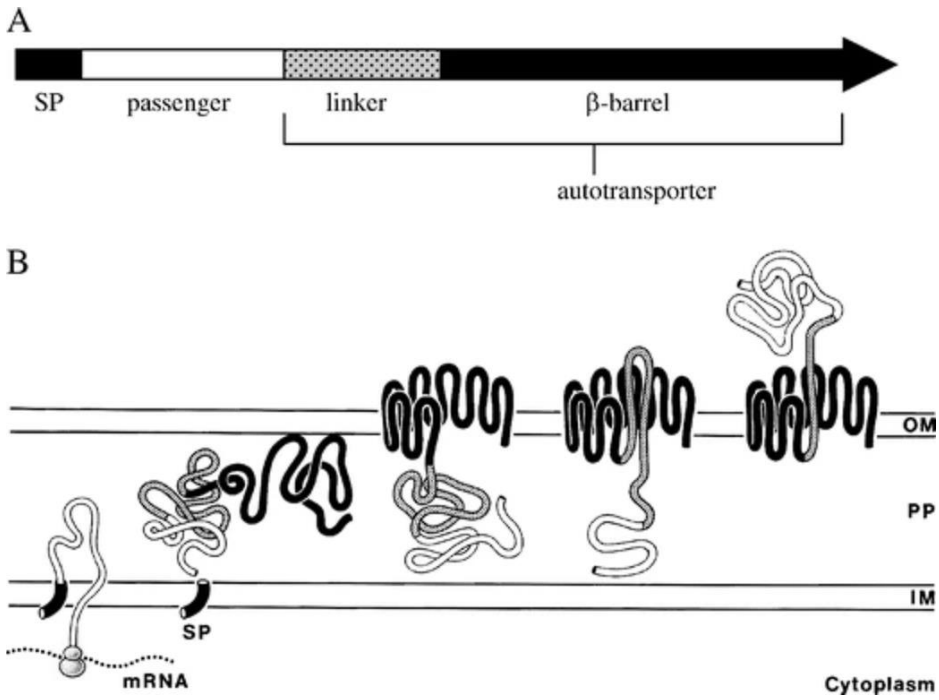

Fig. 2. ***The general structure and function of a classical autotransporter, adapted from the work of Joachim Jose (57) without change. A)*** *The structure of the precursor.* ***B)*** *Either post-translationally or co-translationally, the N-terminal signal peptide (SP) facilitates the Sec-dependent transport of the precursor protein across the inner membrane (IM). In the periplasm (PP), the C-terminal translocation unit folds, creating a β-barrel within the OM, through which the passenger is transmitted to the cell surface.*

The passenger then can either stay attached to the rest of the autotransporter, as in most cases, or dissociate after the cleavage of the polypeptide chain as is the case for the EstA-like subgroup (58). Genetic engineering can be used to disrupt the cleavage site between the passenger and the translocation unit to anchor the passenger to the membrane. By genetically fusing a protein of interest to the passenger domain, these modified autotransporters facilitate the translocation of the fusion partner across the OM, anchoring it to the outer surface. Two examples of Type Va autotransporters that have previously been engineered for bacterial surface display are adhesin involved in diffuse adherence (AIDA-I) and haemoglobin binding protease (Hbp).

Jarmander et al. (59) created a surface display system based on AIDA-I, where the original passenger domain is replaced by a dual tag system composed of an N-terminal His6-tag next to a cleavage site for recombinant type 14 3C protease from human rhinovirus and a C-terminal Myc tag next to a tobacco etch virus protease site. This allowed the authors to use fluorescent antibodies to analyze the surface display of *Salmonella enterica serovar Enteritidis (S. Enteritidis)* flagellar protein H:gm (111 kDa) and fimbrial protein SefA (72 kDa). They found that both proteins could be displayed on the bacterial surface, but the larger H:gm underwent significantly more degradation on its N-terminus. The reason for this is most likely periplasmatic proteolysis as cytoplasmic N-terminal proteolysis would have affected the signal peptide necessary for Sec-mediated translocation, and the bacterial strain used in their experiments did not have any outer membrane proteases that could explain the results.

Haemoglobin binding protease has been extensively researched for bacterial and OMV surface display of heterologous antigens, employing protein ligation systems in multiple cases (6, 60-63). Van den Berg van Saparoea et al. created the HbpD(Δd1) surface display system (60) where the d1 subdomain of the Hbp passenger domain is replaced by a protein fusion partner. Unlike in the AIDA-I based system, the fusion partner in this system is located at the tip of the long, stem-like β-barrel structure of the Hbp passenger domain, relatively far from the membrane surface. The authors show that various antigens can be efficiently displayed using this system, and similarly to AIDA-I based display, larger/bulky fusion partners have been shown to decrease display efficiency.

For radiolabeling, the displayed fusion partner should allow a simple, specific, high yield radiochemical procedure resulting in a highly stable product. It should also be advantageous to be easily adaptable for different radionuclides and bacterial strains. Protein ligation systems, like the SpyCatcher/SpyTag technology (64) offer a possible solution to this challenge. Due to the widespread use of surface display and protein ligation in OMV surface engineering, a radiolabeling method based on these technologies would be easily incorporated into existing solutions (5, 6, 60, 65-67). SpyCatcher (SpC) is a 12.3 kDa protein that forms a spontaneous isopeptide bond with the peptide tag SpyTag (SpT), as illustrated in Fig. 3 (64). Derived from the modified CnaB2 domain of fibronectin-binding protein FbaB

of *Streptococcus pyogenes*, this protein ligation system has been used to create covalent bonds between peptides and proteins both in vitro and in vivo (68, 69). The autotransporter passenger domain can be replaced with either one of the binding partners to create bacteria or OMVs that can bind the other binding partner (6, 60, 70).

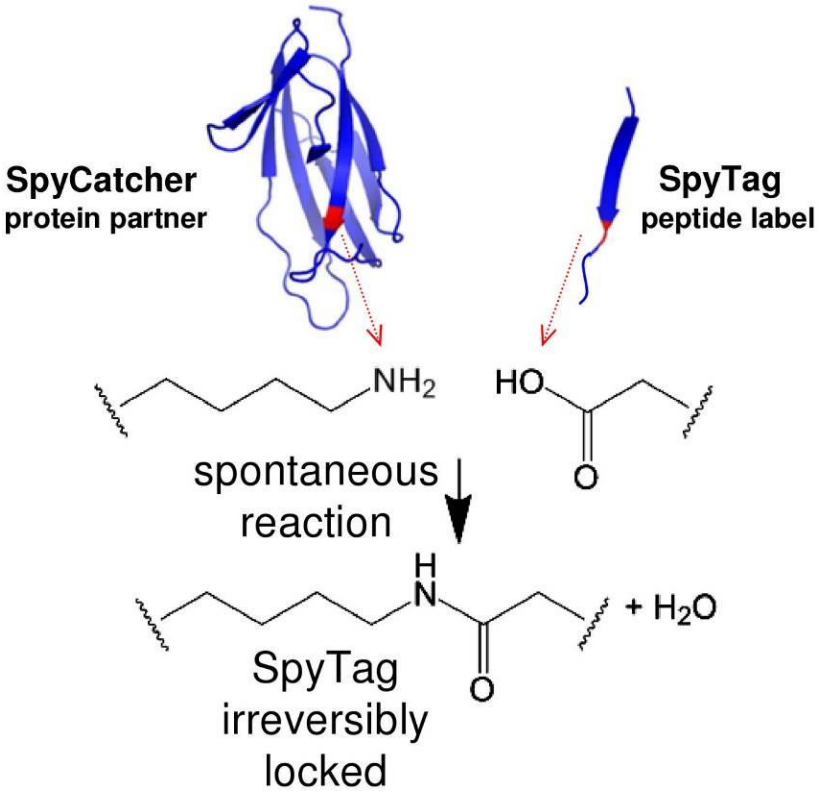

Fig. 3. ***The structure and function of the SpyCatcher-SpyTag protein ligation system, adapted from Zakeri et al. (64) without modification.*** *A covalent bond between the Lys^{31} amine and Asp^{117} carbonyl carbon of the CnaB2 domain spontaneously forms, creating an isopeptide link between SpyCatcher and SpyTag.*

The combination of a surface display system with a protein ligation system enables the decoration of OMVs with proteins that could not be efficiently displayed by direct genetic fusion with the surface display system due to their large size or folding properties. It also makes the surface display of non-peptide molecules possible, therefore allowing the OM anchoring of a chelator for radiolabeling. Further combination with orthogonal protein

ligation systems (e.g. SnoopCatcher/SnoopTag) can be used to create a modular platform allowing complex OMV surface functionalization (69), making these systems promising for targeted drug delivery and vaccine development.

The choice of chelator determines the set of radionuclides that can be used for labeling. And consequently, the choice of radionuclide determines the time window available for imaging and the modality: SPECT for photon-emitters or PET for positron-emitters. Generally, the bidistribution of EVs is measured on the scale of multiple hours to days, therefore, radionuclides with relatively long half-lives are usually used, e.g. ^{111}In for SPECT and ^{64}Cu or ^{98}Zr for PET imaging (53). It is also important, that the labeling reaction does not damage the vesicles. The macrocyclic chelator 1-(1,3-carboxypropyl)-4,7-carboxymethyl-1,4,7-triazacyclononane (NODAGA) can chelate ^{64}Cu, ^{111}In and ^{68}Ga with excellent in vitro and in vivo stability making it a widely used option for radiochemical applications (71, 72). Importantly, the reaction conditions for ^{64}Cu can be very mild (room temperature, with a wide pH range), which is favorable for EV labeling. NODAGA is also commercially available in precursor form.

For a radiolabeling method based on the expression of recombinant proteins, it is favorable to use a bacterial strain that has a phenotype allowing high yield heterologous protein expression. *Escherichia coli* (*E. coli*) is one of the most widely-used lab bacteria with multiple strains developed for optimal protein expression (73). *E. coli* BL21(DE3) and its derivatives are amongst the most popular strains currently used (74). It is a fast-growing strain with no flagella, reduced acetate production and inactive restriction and methylation system. Other particularly useful phenotypic traits are the absence of lon and OmpT proteases, of which the latter can greatly reduce surface display efficiency (75). However, OmpT deletion is a double-edged sword in this case, as it has been shown to reduce OMV production (76). OMV yield, however, can be increased using genetic engineering. For example, it has been demonstrated in previous studies, that the deletion of the *nlpI* gene, which encodes a regulator of peptidoglycan synthesis can lead to the increased production of extracellular vesicles in *E. coli*, most likely due to increased peptidoglycan turnover (77).

A challenge in OMV based pharmaceutical development is the immunogenicity of OMVs resulting from their high LPS content (78, 79). There exist genetic engineering

solutions to ameliorate the endotoxic effects of *E. coli* LPS. One possibility is the deletion of the *lpxM* gene, blocking the myristoylation of LPS, leading to a phenotype with lower endotoxicity in humans (4-6). Even better results have been achieved through the use of multiple gene deletions in the LPS synthesis pathway (80).

2. Objectives

Our goal is to better understand the mechanism by which the host is affected by its microbiota. Although there are a large variety of important mediators and pathways we decided to focus on LPS and OMVs due to their important roles in human pathogenesis and the possible medicinal applications of the latter. Therefore, we aimed to evaluate and develop molecular imaging methods to study the neuroinflammatory effects of LPS and the biodistribution of OMVs.

Our detailed goals are the following:

1. Develop an efficient radiolabeling method for in vivo imaging of OMVs, as summarized in Fig. 4:
    - Use genetic engineering to delete the nlpI and LpxM genes from E. coli BL21(DE3) to create a strain suitable for high yield OMV production and heterologous protein expression while having reduced immunogenicity.
    - Anchor SpyCatcher to the OMV surface using an autotransporter-based surface display system.
    - Create SpyTag-NODAGA-based bifunctional chelators that bind to the SpyCatcher-displaying OMVs, facilitating radiolabeling.
    - Label the OMVs with ^{64}Cu and characterize the radiolabeling.
    - Use PET/MRI to measure the biodistribution of labeled OMVs.
2. Test if [^{125}I]CLINME SPECT can be used to detect early neuroinflammatory changes in a murine model of SAE.

DOI:10.14753/SE.2024.3055

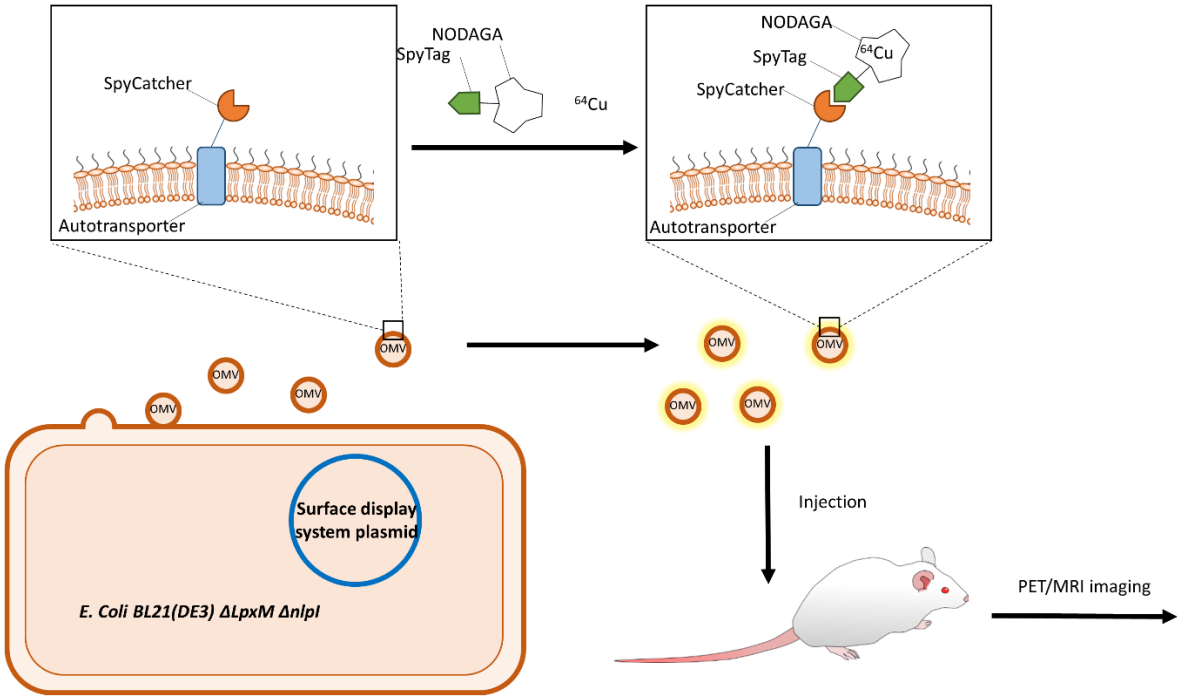

Fig. 4. ***Illustration of the proposed OMV radiolabeling method***. *E. coli BL21(DE3) ΔnlpI, ΔLpxM cells harboring a surface display plasmid express an autotransporter-SpyCatcher fusion protein that integrates into the outer membrane. A synthetic SpyTag-NODAGA bifunctional chelator labeled with 64Cu can covalently bind to the OMV surface with high specificity. The precise biodistribution of these radiolabeled OMVs can be measured using PET/MRI multimodal imaging.*

3. Methods

3.1 Imaging of bacterial OMVs

3.1.1 Culture conditions

For all bacterial liquid cultures lysogeny broth (LB) was used as a medium, prepared using LB Broth (Miller) powder (Sigma Aldrich, USA). LB agar was prepared using 1.5% Select agar powder (Sigma Aldrich, USA). Ampicillin (SERVA Electrophoresis, Germany), kanamycin (SERVA Electrophoresis, Germany), or chloramphenicol (SERVA Electrophoresis, Germany) were used at concentrations of 100 μg/ml, 50 μg/ml, and 34 μg/ml respectively when necessary. Induction of bacteria harboring SpyCatcher surface display plasmids with isopropyl β-d-1-thiogalactopyranoside (IPTG, Thermo Scientific) was carried out at $OD_{600} \approx 0.7$ when required. The final concentration of IPTG was an important parameter in the optimization of surface display, therefore it is described separately for different experiments. Bacteria were cultured for 16 h (following induction) at 37°C with shaking at 180 RPM if otherwise not specified.

3.1.2 Preparation of BL21(DE3) *ΔnlpI, ΔLpxM*

Lambda Red genome editing was used to create two knockout mutations in *E. coli* BL21(DE3) cells (CMC0016, Sigma-Aldrich, USA) following the method described by Sheila Jensen and Alex Nielsen (81). The thermosensitive helper plasmid pSIJ8 (82) (plasmid number: #68122, Addgene, USA) was electroporated into the BL21(DE3) cells with a GenePulser Xcell Electroporation System (Bio-Rad, USA) using a 1 mm electroporation cuvette (Bio-Rad, USA). A time-constant protocol was used with 1.8 kV voltage and 5 ms time-constant. All further electroporations were done using the same setup. FRT-flanked kanamycin resistance cassettes with flanking regions homologous to the downstream and upstream ~50 bp regions of the *nlpI* and *lpxM* genes were PCR-amplified from Keio collection (83) strains (Horizon discovery, UK, *nlpI* mutant: OEC4987-200828301, *lpxM* mutant: OEC4987-213605786) using Q5 High-fidelity DNA polymerase (New England BioLabs, USA). Following purification by agarose gel electrophoresis, gel excision and a Nucleospin PCR cleanup kit (Macherey Nagel, Germany), the PCR products were used to delete the *nlpI* and *lpxM* genes from *E. coli* BL21(DE3) sequentially, starting with the former. Keeping all cultures at 30°C, the lambda-Red genes encoded on pSIJ8 were induced with 20

mM L-(+)-arabinose (Sigma-Aldrich, USA) at OD_{600} ~0.4. Cells were grown for another 45 minutes, then made electrocompetent following the protocol described in (81). A volume of 5 µl of the PCR product with *nlpI* homologous regions was used to transform 50 µl of electrocompetent cells. After electroporation with the PCR products followed by recovery in LB medium, cells were grown on LB plates containing 100 µg/ml ampicillin and 50 µg/ml kanamycin at 30 °C. Colony PCR using Q5 polymerase and the appropriate primer pairs was used to verify successful recombination. A 2-hour culture grown in 1 ml LB with ampicillin and kanamycin was centrifuged at 6500 g, 2 min, RT, resuspending in 1 ml LB with ampicillin, and treated with 50 mM L-rhamnose (Sigma-Aldrich, USA) for 4 hours to induce flippase expression from pSIJ8 leading to the deletion of the FRT-flanked kanamycin resistance cassette. Next, cells were grown on LB plates containing 100 µg/ml ampicillin. To delete the *lpxM* gene from the resulting BL21(DE3) *ΔnlpI* strain, the same procedure was repeated using the PCR product with *lpxM* homologous regions. To remove pSIJ8, cells were grown at 37 °C in LB, then spread on two LB plates - one containing ampicillin - and grown at 37 °C to verify successful removal of the plasmid. Both deletions were verified by PCR and the presence of the remaining FRT scar sequence was verified by sequencing the PCR products. The resulting double mutant BL21(DE3) *ΔnlpI, ΔlpxM* was verified using PCR and sequencing. The novel strains was designated BL21.V (84).

3.1.3 Isolation and characterization of OMVs

3.1.3.1 OMV isolation

OMV isolation consisted of three main steps but the specifics of the protocol depended on the sample size. First, bacterial cultures were centrifuged at 5000 g, 15 min, 4°C and the supernatant was filtered using a 0.45 µm pore size filter. Next, the sterile supernatant was concentrated. For 500 ml samples, concentration consisted of stirred-cell ultrafiltration using a 100 kDa nominal molecular weight polyethersulfone ultrafiltration disc (Millipore, USA) followed by tangential flow filtration using the TFF-easy tangential filtration unit (Hansa Biomed, Estonia) and ultracentrifugation for 2 hours at 150,000 g, 4°C using an XL-80 ultracentrifuge (Beckman-Coulter, USA) equipped with a Type 50.2 Ti rotor. For 25 ml samples only the ultracentrifugation step was used. Following ultracentrifugation the supernatant was discarded and the pellet gently resuspended in either 500 µl (for 500 ml

starting volume) or 250 µl (for 25 ml samples) phosphate buffered saline (PBS) (137 mM NaCl, 2.7 mM KCl, 10 mM Na_2HPO_4, and 1.8 mM KH_2PO_4, pH 7.4) and then filtered using a Costar Spin-X 0.45 µm centrifuge filter (Corning, USA). In the final step the samples were purified using a 2.1 ml size exclusion chromatography (SEC) column packed with Sepharose CL-4B (Cytiva, Germany). Purified OMV samples were quantified according to their protein content measured with the Pierce modified Lowry protein assay kit (Thermo Scientific, USA) using a BSA standard. OMV isolates were stored at 4°C for up to 4 weeks.

3.1.3.2 Sodium dodecyl sulfate-polyacrylamide gel electrophoresis (SDS-PAGE)

SDS-PAGE was used as a general post-isolation quality control step and to analyze OMV surface display of SpyCatcher. The 10% resolving and 5% stacking polyacrylamide gels were prepared in a Mini-Protean Tetra casting stand (Bio-Rad, USA) with a 1 mm spacer. Samples were mixed 1:1 with 2x reducing sample buffer (50 mM Tris-PO_4, pH 6.8; 2% SDS; 2 mM EDTA (Sigma Aldrich, USA); 20% glycerol (Sigma Aldrich, USA); 0.02% bromophenol blue (Sigma Aldrich, USA); 10% 2-mercaptoethanol (Sigma Aldrich, USA) and incubated at 95 °C for 5 minutes unless specified otherwise. For fluorescent OMV samples, the gel was washed 3x with ultrapure water following electrophoresis and scanned using an Amersham Typhoon 9400 (GE, USA). Gels were stained with PageBlue protein staining solution (Thermo Scientific, USA) according to the manufacturer's instructions. A GelLogic 212 Pro (Carestream, USA) system was used to image the PageBlue stained gels.

3.1.3.3 Transmission electron microscopy (TEM)

OMV size distribution was determined using TEM. A 2 µl OMV sample was applied to a Lacey Carbon Type-A copper grid (Ted Pella Inc, USA) and incubated for 2 minutes. The excess suspension was blotted with a piece of filter paper before the grids were placed on a drop of 2% uranyl acetate (v/v) solution for 1 min, blotted, then placed on another drop again for 1 min. After blotting the excess uranyl acetate solution, the grids were air-dried and viewed using a JEOL JEM-1011 TEM (JEOL, Peabody, MA, USA) operated at 80 kV equipped with a Morada TEM 11 MPixel camera from Olympus (Olympus, Tokyo, Japan) using iTEM5.1 software for metadata analysis. OMV size distribution was determined using NIH ImageJ software by manually fitting ellipses around all vesicles. All round or slightly elongated objects with well-defined smooth edges on 3 photomicrographs were included in

the analysis. A total of 529 OMVs were measured this way. Major and minor axis lengths were averaged and a histogram was created using python.

3.1.3.4 Attenuated total reflectance Fourier-transform infrared spectroscopy (ATR-FTIR)

The infrared spectra were recorded with a Bruker Vertex80v (Bruker Optics, Billerica, MA) FTIR spectrometer equipped with a high sensitivity mercury-cadmium-telluride detector. Each spectrum was collected by averaging 128 scans at 2 cm^{-1} resolution. The sample (3 µl) was dried on a single reflection diamond attenuated total reflectance (ATR) crystal. Spectral manipulations were performed using the GRAMS/32 software package (Galactic Inc, USA).

3.1.4 Optimization of SpyCatcher surface display

3.1.4.1 High performance liquid chromatography (HPLC)

Size exclusion HPLC (SEC-HPLC) was generally used for the quality control of OMV isolates and to analyze SpyCatcher-displaying OMVs following fluorescent or radioactive labeling. Reversed-phase HPLC (RP-HPLC) was used to check the quality of synthetic peptides and the results of peptide radiolabeling.

For SEC-HPLC, the Jasco HPLC system was equipped with a PU-2089 pump unit, LC-NET II ADC, UV-2089 UV-Vis detector, Idex 7725i front-loading injector with a 100 µl loop, and a gamma-RAM Model 4 radio-HPLC detector (LabLogic, USA) equipped with a 100 µl cell. Fluorescent measurements were carried out on another JASCO HPLC system equipped with a PU-4180 pump, AS-4050 autosampler, UV-4075 UV-Vis detector, and an FP-2020 fluorescence detector controlled by ChromNAV Ver.2. A Tricorn-5/50 column with a bed volume of ~1 ml (Cytiva, Germany) packed with Sepharose CL-4B (Cytiva, Germany) was used for SEC-HPLC. PBS (pH 7.4) was used as the mobile phase with a 0.5 ml/min flow rate amounting to a total elution time of 5 minutes per chromatogram. UV attenuation was measured at 280 nm. Fluorescence intensity was measured at 578 nm with 546 nm excitation. Fluorescence and UV-attenuation chromatograms were split into two peaks manually to calculate areas under the curves. The first peak corresponded to the OMV fraction. Due to their low signal-to-noise ratio, radio-chromatograms were exported and analyzed by fitting

the two peaks using an exponentially modified Gaussian (EMG) and general exponentially modified Gaussian (GEMG) function (85). Due to the various expressions found within the literature, and to avoid ambiguity, the equations are presented below:

$$\boldsymbol{GEMG(t) = \frac{A}{1+b}(EMG_1 + bEMG_2)} \quad \text{Eq. 1.}$$

Where

$$\boldsymbol{EMG_i(t) = e^{q_i} I_i/\tau_i} \quad \text{Eq. 2.}$$

$$\boldsymbol{q_i = \frac{\sigma^2}{2\tau_i^2} - \frac{t - t_m}{\tau_i}} \quad \text{Eq. 3.}$$

$$\boldsymbol{I_i = \Phi(z_i)} \quad \text{Eq. 4.}$$

$$\boldsymbol{z_i = \frac{t - t_m}{\sigma} - \frac{\sigma}{\tau_i}} \quad \text{Eq. 5.}$$

Where t is time, A is area, b is the parameter determining the mixing of the second EMG function, σ and t_m are the standard deviation and expected value of the common Gaussian component of the two EMG's respectively, τ_i are the rate parameter of the ith exponential distribution and Φ is the cumulative density function of the normal distribution. The initial parameters and their bounds were determined on chromatograms of purified OMV samples. The first peak was modeled with an EMG function and tight constraints were used on the shape and location parameters (τ_1, σ, t_m). The second peak was modeled with a GEMG function. The lower constrain for the ratio of τ_i / σ was set to 0.2 to avoid numerical errors. The Levenberg-Marquardt algorithm was used to find the optimal parameters of the two-peak model. All optimizations were repeated 5 times with random initial parameters to avoid local minima. All results were visually evaluated for incorrect fitting.

For RP-HPLC, a Chromolith FastGradient RP-18e 50-2 mm column (Supelco, USA) was used. MilliQ water with 0.1% trifluoroacetic acid (Solvent A) and 100% acetonitrile (Solvent B) were used as mobile phases. A sample volume of 1 µl was used and the gradient elution protocol was the following: 0-1 min: 100% Solvent A, 1-9 min: 0-80% Solvent B, 9-12 min: 80%-0% Solvent B, 15-20 min: 100% Solvent A. A flow rate of 0.360 ml/min was used. UV absorbance was measured at 220 nm. For radioactivity measurements, the radio-HPLC detector was equipped with a 25 µl cell.

3.1.4.2 Synthesis of labeled SpyTag variants

We synthetized both fluorescent and chelator-conjugated SpyTag variants to analyze OMV SpyCatcher display and to carry out the radiolabeling procedure. Synthesis of SpyTag (AHIVMVDAYKPTKGGGK) and its elongated (ATKGDAHIVMVDAYKPTKGSGGK) analogue peptide was carried using Fmoc/tBu strategy (84). Orthogonally protected lysines were used to synthesize fluorescent SypTag peptide derivative (SpT-CF) by conjugating the C terminal lysine of the original SpyTag peptide with carboxifluorescein. SpT-3-NODAGA and SpT-23-NODAGA were obtained by NODAGA labeling of elongated Spytag variants (with either Boc-protected K3 or K23, respectively) using NODAGA-NHS (Chematech, Dijon, France). The crude products were purified using HPLC. The identification of the products was achieved by mass spectrometry and the purity of the products was determined using reversed-phase HPLC.

3.1.4.3 Construction of surface display plasmids

To anchor SpyCatcher to the OM, we created two different SpyCatcher-autotransporter fusion proteins based on AIDA-I and Hbp. First, the *SpyCatcher* gene was inserted into pAIDA1 (59) (plasmid number: #79180, Addgene, USA) between the XbaI and SalI restriction sites, and into pHbpD(Δd1) (60) (a gift from Abera Bioscience) between the SacI and BamHI restriction sites using restriction cloning to create the plasmids pAIDA-SpC and pHbpD-SpC respectively (84). The resulting fusion genes (*AIDA-SpyCatcher* and *HbpD-SpyCatcher*) were then inserted into the pET28a vector between the NcoI and SacI sites in the case of *AIDA-SpyCatcher* and between the NcoI and NheI sites in the case of *HbpD-SpyCatcher* to create the plasmids pET28-ASpC and pET28-HSpC respectively. All four plasmids were used to transform different batches of *E. coli* BL21.V cells using electroporation. Transcription from these plasmids in *E. coli* BL21.V are inducible using IPTG. The fusion genes are illustrated in Fig. 5.

DOI:10.14753/SE.2024.3055

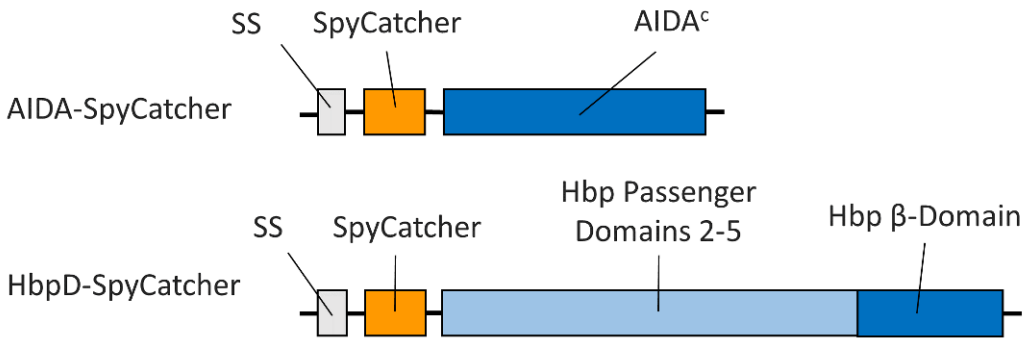

Fig. 5. ***Illustration of the SpyCatcher-autotransporter fusion genes.*** *SS: signal sequence that directs the proteins to the outer membrane. AIDA^c: C-terminal transmembrane domain of AIDA-I. Hbp β-Domain: C-terminal transmembrane domain of Hbp.*

3.1.4.4 Evaluating SpyCatcher surface expression on bacteria

Flow cytometry (FCM) was used to evaluate bacterial surface display of SpyCatcher after SpT-CF labeling. Liquid cultures of BL21.V (empty, or harboring surface display plasmids) were grown in LB supplemented with the necessary antibiotics at 37 °C, 180 RPM shaking until OD_{600} ~0.7, divided into 5 ml batches and IPTG (0, 40, 400, 2000 µM) was added to induce protein expression. Following the addition of IPTG, the cultures were incubated for 16 hours at 24 °C or 37 °C shaking at 180 RPM. Final OD_{600} was measured with a NanoDrop 1000 spectrophotometer (Thermo Scientific, USA). Depending on the OD_{600} values, a volume of 80-200 µl of the culture was diluted in 800 µl PBS and centrifuged at 5000 g, 4°C for 10 min. The supernatant was removed, then the pellets were resuspended in PBS containing 10 µM SpT-CF and incubated for 1 h at room temperature on an orbital shaker. Next, the samples were washed three times by adding 800 µl PBS, centrifuging at 5000 g, 4°C for 10 min and discarding the supernatant. The pellets were finally resuspended in 400 µl PBS and transferred to round bottom plastic tubes (Sarstedt, Germany). FCM measurements were carried out using a FACSCalibur (BD Biosciences, USA) flow cytometer. FlowJo v. 10 (BD biosciences, USA) was used to define gates for *E. coli* on a log-log forward scatter/side scatter plot. Fluorescence data measured on the FL1 channel was

exported as CSV files and loaded into python using pandas (86) and plotted using seaborn (87) and matplotlib (88). A Kruskal-Wallis test with Dunn's post-hoc test was used to compare the fluorescence of samples from the selected induction protocol (40 μM IPTG, 37 °C).

To investigate irregularities on the FCM scatter plots, samples were then loaded onto a coverslip after FCM measurement and phase-contrast photomicrographs were created using a Nikon Eclipse Ti inverted microscope.

3.1.4.5 Evaluating SpyCatcher expression on OMVs

SpyCatcher display on the OMV surface was quantified using SDS-PAGE and SEC-HPLC following SpT-CF labeling. SpT-CF (2 mM) was diluted in OMV samples isolated from BL21.V (empty, or harboring surface display plasmids), to a final concentration of 10 μM and the mixture was incubated for 24 h at 4 °C on an orbital shaker. For SEC-HPLC, the percentage of the area under the peak of the OMV fraction on the fluorescent chromatogram was divided by the area of the same peak on the UV chromatogram. For SDS-PAGE, the integrated fluorescent intensity of SpyCatcher-bound SpT-CF bands was divided by the integrated density of OmpF bands following PageBlue staining. Measurements were carried out on 3 separate OMV isolates for each plasmid.

3.1.4.6 Evaluating SpT-NODAGA binding on OMVs

A simplified binding assay was used to compare the affinity of SpT-3-NODAGA and SpT-23-NODAGA to SpyCatcher-displaying OMVs. A volume of 19 μl SpyCatcher-displaying OMV (1.75 mg/ml) was incubated with 10 μM of each SpT-NODAGA variant (or MilliQ water for the negative control) at 4 °C on an orbital shaker. After 24 hours, SpT-CF was added at a final concentration of 10 μM and the mixtures were further incubated for 24 hours. Following incubation, SDS-PAGE was used to resolve specifically bound SpT-CF. The fluorescence intensity of the band corresponding to [AIDA-SpC]-[SpT-CF] was quantified and normalized to the density of the OmpF band measured after PageBlue staining. Measurements were carried out on 3 separate OMV isolates for each peptide.

DOI:10.14753/SE.2024.3055

3.1.5 Radiolabeling OMVs

Two different methods were evaluated for OMV radiolabeling, as illustrated in Fig. 6 and detailed below.

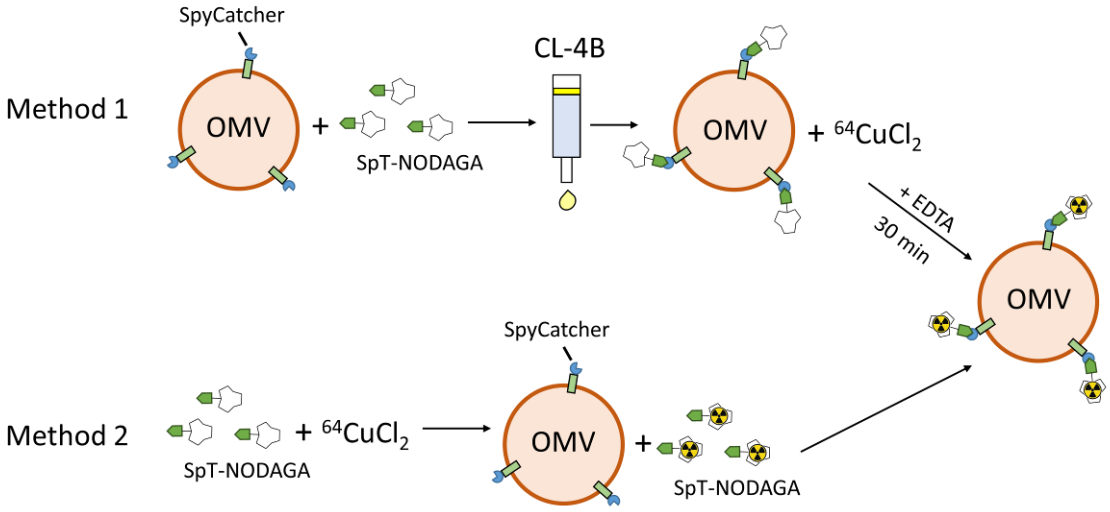

Fig. 6. ***OMV radiolabeling methods.*** *In Method 1, the reaction between SpyCatcher-displaying OMVs and SpT-NODAGA takes place first, followed by removing unreacted SpT-NODAGA and labeling with ^{64}Cu. In Method 2, the order of these steps are reversed, first SpT-NODAGA is labeled using ^{64}Cu, then mixed with SpyCatcher-displaying OMVs.*

In *Method 1* SpyCatcher-displaying OMVs (1.6 mg/ml) were incubated with 5 µM of each SpT-NODAGA variant for 24 hours at 4°C on an orbital shaker. Following incubation, free peptides were removed using a 2.1 ml Sepharose CL-4B gravity column eluted with sodium acetate buffer (0.1 M, pH=6.0). A volume of 300 µl of the resulting OMV suspension was mixed with 142.5 ± 0.7 MBq $^{64}CuCl_2$ (produced at the Helmholtz-Zentrum Dresden-Rossendorf, Germany, ~12 MBq/µl at the start of experiments) and adjusted to a final volume of 340 µl. The mixture was incubated for 20 minutes at 37 °C 300 RPM shaking. The reaction was stopped by adding 2 mM Na-EDTA to the mixture followed by 15 min incubation at room temperature. Radiochemical purity (RCP) was measured with SEC-

HPLC. Free ^{64}Cu was removed using a 2.1 ml Sepharose CL-4B column with PBS (pH = 7.4) as the equilibration buffer. Fractions (200 µl) were collected in individual tubes and radioactivity was measured using an ISOMED 2010 dose calibrator (Nuvia, France). The two fractions with the highest activity were pooled. For serum stability measurements 20 µl of the pooled OMV sample was mixed with 80 µl fetal bovine serum (Thermo Fisher, USA) and incubated at 37 °C 300 RPM shaking. The samples were analyzed with SEC-HPLC at 3, 4, 8, 12 and 24 h post-incubation.

In *Method 2,* SpT-3-NODAGA and SpT-23-NODAGA were first labeled with ^{64}Cu in sodium acetate buffer (0.2 M, pH = 6.0). Peptides were diluted to a final concentration of 40 µM and 109.28 ± 0.78 MBq $^{64}CuCl_2$ was added to the mixture for each nmol of peptide. The reaction mixtures were incubated for 20 minutes at 37 °C 300 RPM shaking. The reaction was stopped by adding 2 mM Na-EDTA to the mixture followed by 5 min incubation at room temperature. Radiochemical purity was assessed using RP-HPLC. Radiolabeled peptides ([^{64}Cu]SpT-3-NODAGA and [^{64}Cu]SpT-23-NODAGA) at a final concentration of 5 µM were mixed with SpyCatcher-expressing OMVs (1.6 mg/ml) in PBS and incubated at 37 °C 300 RPM shaking. Radiochemical purity was measured with SEC-HPLC at 1, 2, and 4 hours post-incubation. For negative control, OMVs from the same isolates were pre-incubated with 10 µM SpT-CF for 24 h at 4 °C on an orbital shaker to block available SpyCatcher binding sites. This experiment was repeated on three different OMV isolates.

3.1.6 In vivo imaging of OMVs

Four healthy 21-week-old male BALB/c mice (body weight = 24.73 ± 3.88 g) were used for the biodistribution studies. A volume of 120 µl radiolabeled sample (radiolabeled SpT-3/23-NODAGA or OMVs) with an activity of 10.17 ± 1.10 MBq (Mean ± SD) was administered intravenously into the lateral tail vein. One mouse was used per sample. Mice were anesthetized with isoflurane (3.5-4% induction, then reduced to 1.5% for the maintenance of anesthesia during imaging) for the whole duration of imaging. PET/MRI acquisitions were carried out using a nanoScan PET/MRI 3T (Mediso, Hungary) equipped with a Mediso mouse whole-body coil resulting in a 3D PET resolution of 1.4 mm at full width at half maximum (FWHM) and a PET sensitivity of 200/s true detection rate per kBq. A GRE 3D sequence with a 45° flip angle, 15 ms repetition time, and 4.2 ms echo time with

2 excitations averaged was used to acquire 64 coronal slices with a slice thickness of 0.4 mm and an in-plane resolution of 0.33 mm. PET images were acquired 3h, 6h, and 12h post-injection (p.i.) from the 400-600 keV energy window using an acquisition time of 5 min and a 5 ns coincidence time window. The Tera-Tomo 3D (Mediso, Hungary) algorithm with MRI-based attenuation and scatter correction, normal regularization, median and spike filter, and edge-artifact reduction was used to reconstruct the images with 2 iterations and 6 subsets resulting in 0.6 mm isovoxel size. Images were analyzed using vivoquant 1.22 (inviCRO, US). Volumes of interest (VOI) were manually delineated around selected organs (brain, lungs, heart, liver, spleen, kidneys, bladder, and intestines). VOI uptake data are reported in mean standardized uptake values (SUV_{mean}). 3D Slicer 4.11 (89) was used to create figures for illustration.

3.1.7 Data analysis

Microsoft Excel and Python 3.7.12 was used to process and analyze most data and plot graphs. The Python package SciPy (90) was used for statistical hypothesis tests.

A linear mixed-effects model with random intercepts (for each sample) in R (v. 4.1.1.) (91) using the package nlme (92) was used to analyze serum stability data.

Numeric results are presented as mean ± standard deviation when applicable unless otherwise noted.

3.2 Systemic inflammation

3.2.1 Animals

Experiments with [^{125}I]CLINME were performed in mice bred in the Animal House of Semmelweis University. Animals were allowed free access to food and water and maintained under temperature, humidity and light-controlled conditions. All procedures were conducted in accordance with the ARRIVE guidelines and the guidelines set by the European Communities Council Directive (86/609 EEC) and approved by the Animal Care and Use Committee of the IEM and the Semmelweis University (XIV-I-001/29-7/2012).

3.2.2 SAE model

Six adult female C57BL/6 mice (n=3 control, body weight = 30.35 ± 2.7 g; and n=3 LPS-treated, body weight = 29.23 ± 0.64 g) were used to evaluate [^{125}I]CLINME for the

detection of early neuroinflammatory signs in SAE. The SAE model was induced by 3.3 mg/kg body weight of LPS (serotype: 0111:B4, Sigma-Aldrich, St. Louis, MO, USA, L4391) via tail vein injection.

3.2.3 [^{125}I]CLINME preparation

CLINME molecules (precursor synthesis by Progressio's own process) were radiolabeled using 195.7 MBq [^{125}I]NaI by the classic chloramine-T method. Freshly prepared 90 uL 0.3 M PBS, 60 uL 2mg/mL chloramine-T (Sigma-Aldrich, St. Louis, MO, USA), and 30 uL 0.05 M CLINME (Progressio, Hungary) were mixed and incubated for 10 minutes at 90°C. The labeling reaction was stopped by 60 uL 0.1 M Na2S2O3 (Sigma-Aldrich, USA) and purified via Sep Pak plus C18 (Waters Corporation, USA). The specific activity of the product was 28.00 GBq/mmol, the activity concentration was 50.00 MBq/ml and the radiochemical purity was 95%.

3.2.4 In vivo imaging in the SAE model

Mice were anesthetized with isoflurane strictly adhering to our protocol in all cases (3.5-4 % induction and then reduced to 1.52 % for maintenance of anesthesia during scanning). Before imaging 9.53±0.55 MBq (mean±SD) [^{125}I]CLINME was administered intravenously following the subcutaneous injection of 14 mg/kg body weight of potassium perchlorate (Sigma-Aldrich, USA).

SPECT/CT acquisition started 5 h following LPS injection. During the acquisitions mice were placed in prone position in a dedicated mouse bed. Body temperature was monitored and maintained at 37±1 °C. SPECT/CT (NanoSPECT/CT Silver Upgrade, Mediso Ltd., Budapest, Hungary) measurements were performed with multi-pinhole mouse collimators.

The helical CT scans were acquired with 55 kV tube voltage, 500 ms exposure time, 1:4 binning and 360 projections in 3 minutes. In the reconstruction 0.2 mm in-plane resolution and slice thickness were set and Butterworth filter was applied.

Head SPECT scanning was performed with 20 frames per cycle and termination condition of 120 seconds per frame in a scan range of 26.8 mm resulting in a 40-minute scan. The detection peak energies were set to 24 keV with a 20% wide symmetric energy window. SPECT reconstruction was performed with 0.2 mm isovoxels while the field of view was

centered to the head.

Magnetic resonance imaging measurements were performed on nanoScan® PET/MRI (Mediso Ltd., Hungary) equipped with an actively shielded 450 mT/m gradient and volume coils for both reception and transmitting. As anatomic imaging a T2-weighted fast spin echo sequence was acquired with a three-dimensional acquisition scheme having a 42 mm^2 axial field of view and 0.3 mm in-plane resolution, the same as the slice thickness. Imaging parameters were: repetition time/echo time 2200/92.8 ms, 25 μs dwell time and two excitations resulting in a 35-minute acquisition.

Brain segmentation into 3D volumes of interest (cerebrum – indicates the whole brain without cerebellum –, cerebellum, cerebral cortex and hippocampus) was performed using a connected threshold algorithm based on MRI image volumes after coregistration with SPECT/CT images in VivoQuant software (inviCRO, US). The results of SPECT measurements were quantified in units of radioactivity measured per unit volume (MBq/ml). The radioactivity concentrations of the segmented brain areas were presented as a ratio to the injected radioactivity. Normality of data sets was assessed with the Kolmogorov-Smirnov test. Data from in vivo measurements (PET and SPECT scans) were analyzed with the one-sided permutation test.

4. Results

4.1 Imaging of bacterial OMVs

4.1.1 Characterization of *E. coli* BL21.V OMVs

OMV size distribution was determined using crude OMV samples without purification to avoid a possible bias that could be introduced by filtration (Fig. 7). TEM images after negative staining show the typical cup-shaped appearance of extracellular vesicles, (Fig. 7. A) similar to previously reported *E. coli* OMVs (78, 93, 94). After manually fitting ellipses around the vesicles and calculating the mean of minor and major axes, the results (Fig. 7. B) reveal an average OMV diameter of 22.22 ± 9.02 nm.

The typical SDS-PAGE pattern of BL21.V OMVs is shown in (Fig. 7C). OmpF (marked by a red asterisk) is the most abundant OM protein of BL21.V and the intensity of

the OmpF band compared to all other bands was used as a quick quality control to assess the overall purity of OMV isolates.

After SEC purification, we analyzed the samples using ATR-FTIR (Fig. 7. D). Characteristic bands of proteins and lipids can be identified in the spectrum. The bands around 3280, 1645, and 1543 cm^{-1} correspond to amide A, amide I, and amide II vibrations, respectively of the peptide backbone. The presence of lipid is confirmed by the methylene stretching of acyl chains at 2922 cm^{-1} and 2852 cm^{-1} and by the glycerol carbonyl stretching at 1736 cm^{-1} of the phospholipids. From the area of amide I (fitted by a Gaussian function) and the C-H stretching region (integrated from 3020 to 2800 cm^{-1}) a spectroscopic protein-to-lipid ratio (P/L_{spectr}) of 1.57± 0.09 was calculated. Furthermore, the intensity of the amide I can be correlated to the protein concentration of EVs. Applying the protocol elaborated by Szentirmai et al (95), we obtained a total protein concentration of 0.63±0.06 mg/mL for the purified OMVs.

DOI:10.14753/SE.2024.3055

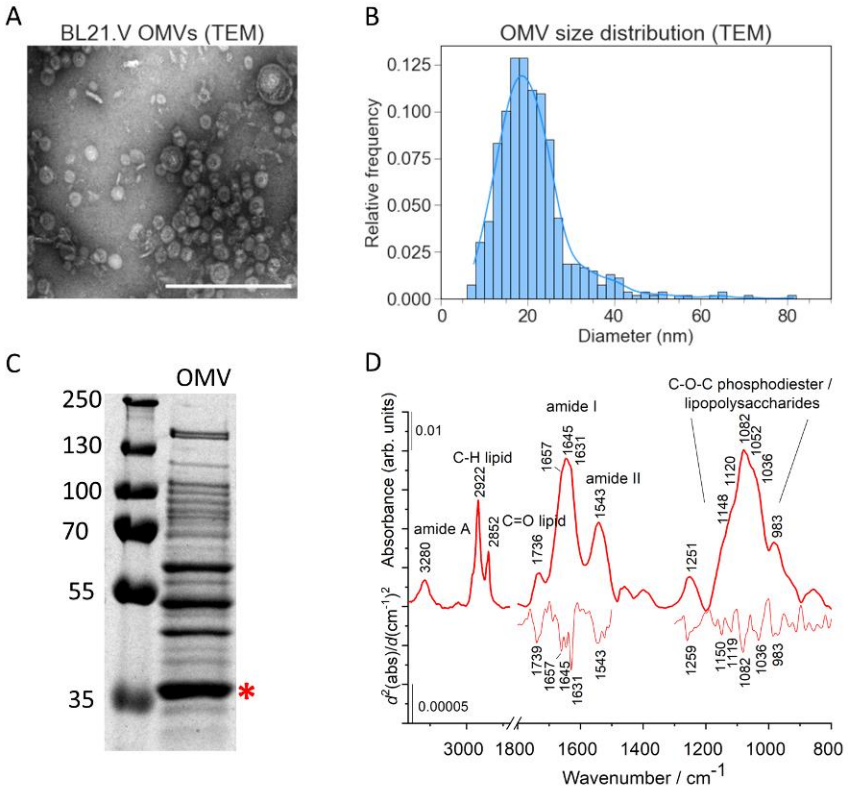

Fig 7. ***OMV characterization results****. **A)** TEM photomicrograph of a crude OMV suspension. The scale bar represents 200 nm. **B)** Size distribution of OMVs measured on TEM images. Bars represent the histogram; the solid blue line is the result of kernel density estimation. **C)** SDS-PAGE of crude OMV sample stained with PageBlue. Red asterisk indicates OmpF band. D) IR spectrum of an OMV sample. To enhance the spectral information, second derivatives of selected wavenumber regions (amide I and amide II from 1800 to 1500 cm-1, and the fingerprint region from 1300 to 800 cm-1) are also shown.*

4.1.2 Optimization of SpyCatcher surface display

Four different plasmids, two AIDA-I-based (pAIDA-SpC and pET28-ASpC) and two Hbp-based (pHbpD-SpC and pET28-HSpC) were evaluated for SpyCatcher surface display. First, SpyCatcher display was measured on bacteria using SpT-CF and FCM. To find the optimal growth conditions, different temperatures (24 °Cand 37 °C) combined with different

IPTG concentrations (0, 40, 400, 2000 μM) were investigated (Fig. 8). Generally higher concentrations of IPTG did not lead to notable increase in SpT-CF binding. Instead, formation of distinct populations on the FSC/SSC plot with different expression levels within the culture, associated mainly with higher IPTG concentrations and lower temperature was observed (e.g. the multimodal fluorescence intensity distribution of pET28-HSpC harboring bacteria induced with 400 μM IPTG at 24 °C in Fig. 8. C, further analyzed in Fig. 9 D, E). Moreover, a tail on the FSC/SSC plot, corresponding to both higher FSC and SSC values was also observable in the case of HbpD-SpC based plasmids in multiple growth conditions. An example is highlighted in Fig. 9. F. To further investigate the cause of the tail we imaged selected samples using phase-contrast microscopy. Cellular aggregation was observable in the case of pHbpD-SpC harboring cells at 24 °C induced with ≥40 μM IPTG and at 37 °C induced with 40-400 μM IPTG. In the case of pET28-HSpC harboring cells, aggregation was observable at 24 °C ≤40 μM IPTG and 37 °C ≤400 μM IPTG. Cellular elongation was also visible in some cases most notably in the case of pET28-HSpC induced with 2000 μM IPTG at 37 °C. These findings correlate well with the appearance of the tail on the FCM scatter plots. An example is demonstrated in Fig. 9. A,B,C,F,G. Based on these FCM results we have decided to continue all further experiments using 40 μM IPTG for induction at 37 °C, as this resulted in unimodal intensity distributions representing relatively high expression levels and the least amount of aggregation in Hbp-based plasmids and no morphological changes.

DOI:10.14753/SE.2024.3055

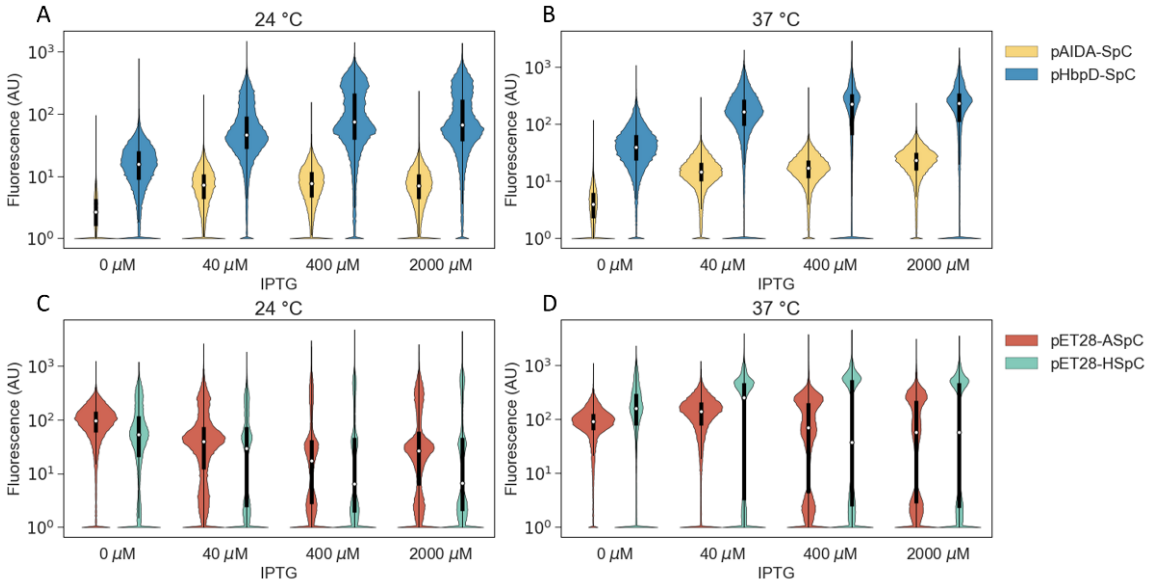

Fig. 8. ***Violin plots showing the fluorescent intensity distributions of SpyCatcher-displaying BL21.V cells labeled with SpT-CF.*** *The white dot of the central boxplot represents the median. Violin plots are scaled to have the same width. Each color corresponds to a different surface display system. The category axis corresponds to different IPTG concentrations used for induction. Subplots represent the growth temperature. The formation of subpopulations with different expression levels is notable, e.g. at 2000 μM IPTG for pHbpD-SpC, pET28-ASpC and pET28-HSpC (sublots A and C).*

DOI:10.14753/SE.2024.3055

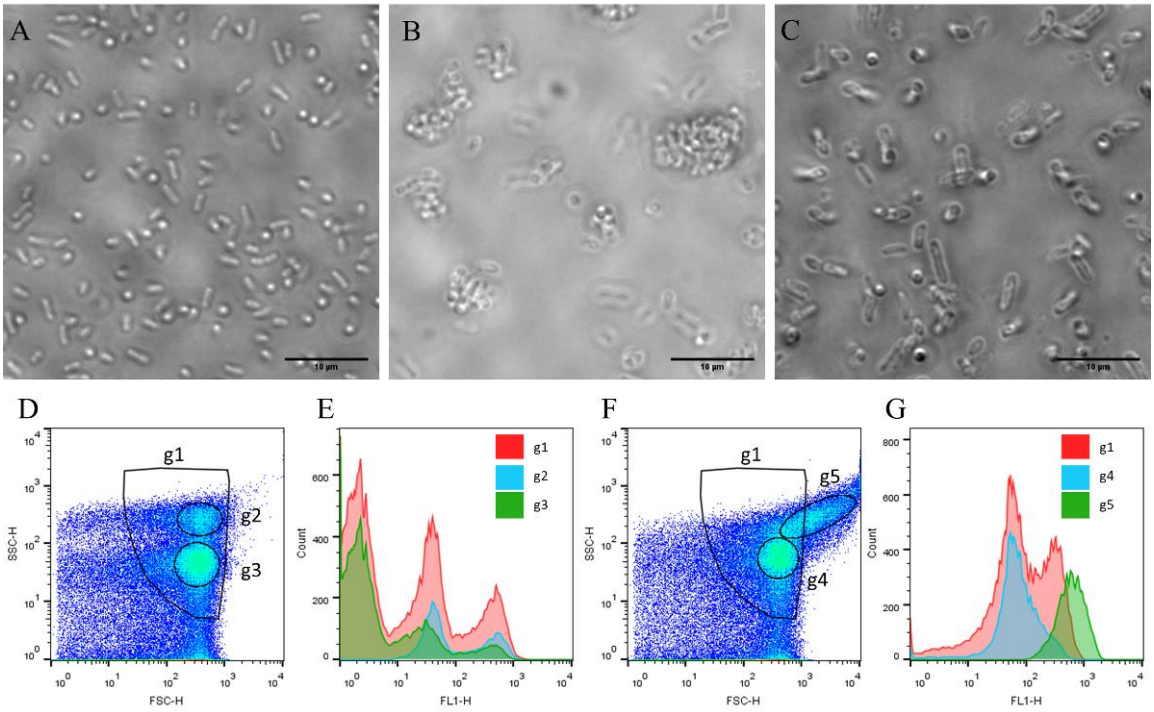

Fig. 9. ***Examples of unwanted cellular changes following IPTG induction.*** *Phase-contrast microscopic images showing different levels of aggregation and morphological changes.* ***A)*** *Normal cellular morphology with no signs of aggregation (pHbpD-SpC, 0 µM IPTG, 24°C).* ***B)*** *High levels of aggregation is observable (pHbpD-SpC, 400 µM IPTG, 24°C).* ***C)*** *Elongated cells (pHbpD-SpC, 2000 µM IPTG, 37°C). All scale bars correspond to 10 µm.* ***D)*** *Flow cytometry FSC/SSC scatter plot of BL21.V harboring pET28-HSpC induced with 400 µM IPTG at 24 °C showing two distinct populations.* ***E)*** *Fluorescence intensity histograms corresponding to the gates defined on the same sample show different intensity distributions for the two populations.* ***F)*** *Flow cytometry FSC/SSC scatter plot of BL21.V harboring pHbpD-SpC induced with 400 µM IPTG at 24 °C showing a tail indicated by g5.* ***G)*** *Fluorescence intensity histograms corresponding to the gates defined on the same sample.*

We also compared the surface display systems based on their effect on OMV yield, as heterologous OM protein expression could in theory affect OMV formation. OMVs were obtained from 25 ml BL21.V cultures harboring each plasmid (and plasmidless bacteria) without purification. OMV yield was determined by SEC-HPLC by measuring the area under

the first peak on the chromatogram. The results are summarized in Fig. 10. Although the results did not reveal any significant differences between the plasmids (Kruskal-Wallis p=0.06) an observable decrease in OMV yield was associated with pET28-ASpC OMVs (AUC = 1.80 ± 0.210 AU for plasmidless vs 0.598 ± 0.395 AU for pET28-ASpC OMVs). The HPLC data was in line with the visibly smaller size of the OMV pellets from pET28-ASpC harboring bacteria during isolation.

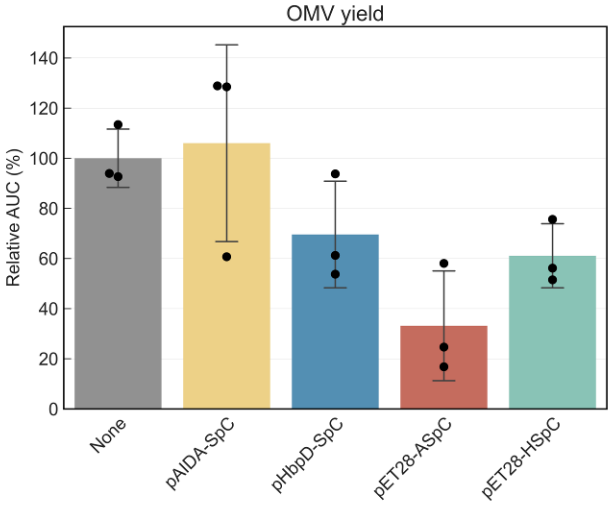

Fig. 10. ***OMV yield measured with HPLC.*** *Bars represent mean, error bars represent standard deviation, swarm plot represents individual measurements. The area under the first peak (OMV fraction) of the SEC-HPLC UV chromatogram was measured. Data is represented relative to OMV yield of the plasmidless bacteria.*

To prove the presence of SpyCatcher on the OMV surface, we carried out fluorescent SDS-PAGE analysis with SpT-CF labeled OMVs. Our results revealed SpT-CF bands at the expected locations of AIDA-SpC and HbpD-SpC fusion proteins (65.896 kDa and 127.780 kDa respectively, Fig. 11. A). These bands were also distinctly visible on PageBlue-stained gels. Further bands most likely corresponding to proteolytic decay were also visible, on the fluorescent gels especially in the case of HbpD based constructs. Interestingly, a double band around 130-150 kDa was also visible in the case of both AIDA-based constructs. This band was also visible in purified OMV samples and was resistant to treatment with urea or trichloroacetate (Fig. 11. B) and showed similar temperature-dependent mobility to AIDA-I

(96) (Fig. 11. C). Western blot analysis of OMVs isolated from BL21.V harboring pAIDA1 with 6x His-tag antibodies revealed no extra bands in this location (Fig. 11. D).

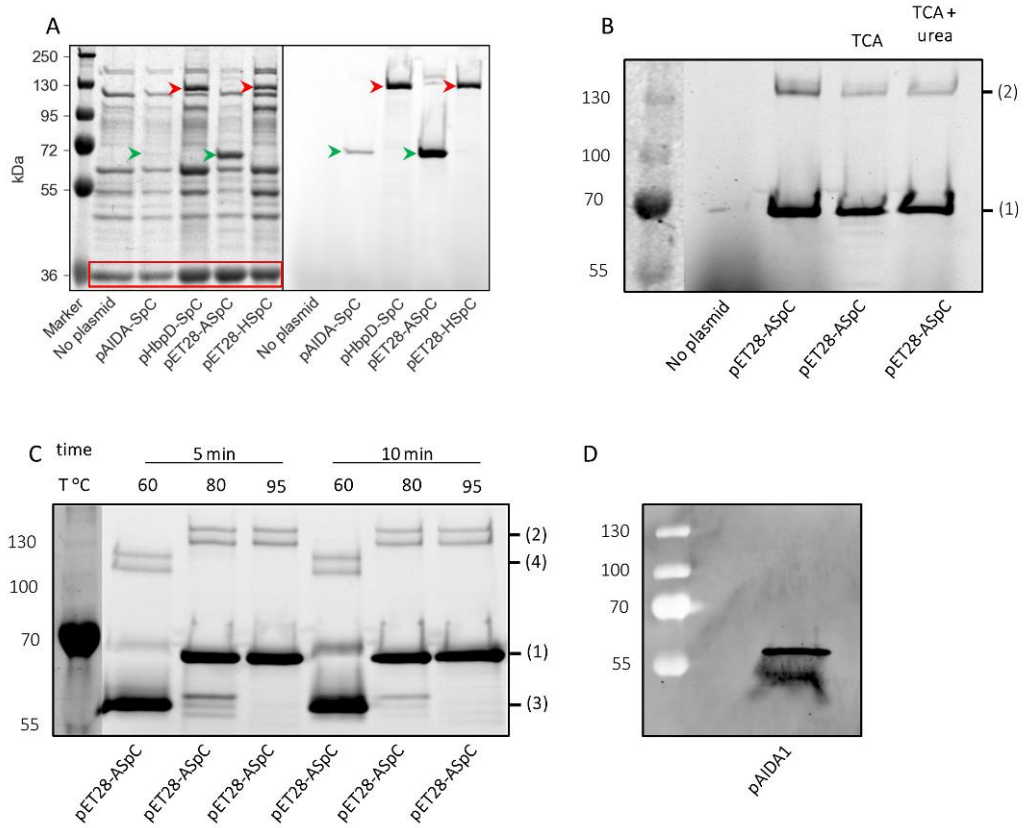

Fig. 11. ***SDS-PAGE analysis of SpyCatcher-displaying OMVs. A)*** *SDS-PAGE of OMVs isolates labeled with SpT-CF. The left image shows the protein bands following PageBlue staining. The OmpF band used as loading control in the next experiments is highlighted with a red rectangle. The right image shows SpT-CF fluorescence on the same gel. Green arrowhead: [AIDA-SpC]-[SpT-CF], red arrowhead: [HbpD-SpC]-[SpT-CF].* ***B)*** *During sample preparation, 10% trichloroacetic acid (TCA) or 10% TCA + 8 M urea was added to the mixture before heating to 95°C for 5 minutes and loading onto a 10% polyacrylamide gel. OMVs isolated from a plasmidless culture show no SpT-CF binding. An unidentified band (2) is observable with approximately twice the MW of AIDA-SpC (1).* ***C)*** *The unidentified band (2) displays similar heat modification properties to AIDA-SpC (1) when the duration and temperature of the heating step of the sample preparation is varied resulting in a shift towards an apparently smaller MW (3 and 4).* ***d)*** *OMVs were isolated from BL21.V*

harboring pAIDA1. The unidentified band is not observable on a Western blot labeled with a fluorescent anti-His antibody. The MW markers of ***B)*** *and* ***C)*** *are visualized on a separate channel of the same scan.*

To find out which plasmid leads to the highest SpyTag binding capacity on the OMV surface, we analyzed SpT-CF labeled OMVs with both fluorescent SDS-PAGE and SEC-HPLC. There was a significant difference between the SpT-CF binding in different plasmid groups (Kruskal-Wallis p=0.024 for SDS-PAGE and p=0.016 for HPLC, Fig. 12). Dunn's post-hoc test with Sidak's correction revealed that OMVs from pET28-ASpC harboring bacteria had significantly higher SpT-CF binding than pAIDA-SpC OMVs based on both methods (HPLC: 2.94 ± 0.33 AU vs 100 ± 48.86 AU, SDS-PAGE: 21.08 ± 10.53 AU vs 100 ± 50.25 AU for pAIDA-SpC and pET28-ASpC respectively, p=0.013 for both comparisons). Based on these results we chose pET28-ASpC for our radiolabeling experiments assuming that the highest SpyCatcher expression would lead to the highest specific activity.

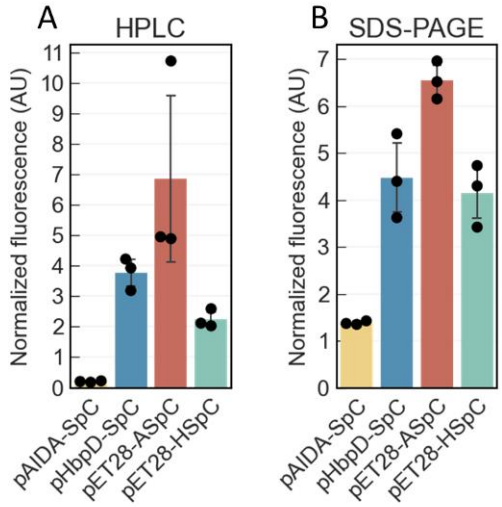

Fig. 12. ***SpT-CF binding of SpyCatcher-displaying OMVs. A)*** *HPLC measurements show that OMVs from pET28-ASpC harboring bacteria bind the highest amount of SpT-CF compared to other plasmids.* ***B)*** *This is supported by SDS-PAGE measurements.*

4.1.3 Radiolabeling of OMVs

We designed two different chelator-conjugated SpyTag variants, SpT-3-NODAGA and SpT-23-NODAGA. By preincubating pET28-ASpC OMVs with either variant before SpT-CF labeling, then measuring the normalized fluorescence intensity using SDS-PAGE, we found that preincubation leads to significantly lower fluorescence for both variants compared to control. Furthermore, fluorescence was significantly lower for SpT-3-NODAGA than SpT-23-NODAGA (85.95% ± 0.85% and 77.28% ± 1.81% respectively, p=0.006, Welch's t-test, Fig. 13). First of all, this shows that both variants can bind to the SpyCatcher displayed on the OMV surface. Secondly, this indicates that SpT-3-NODAGA can inhibit SpT-CF binding better, suggesting more favorable kinetics.

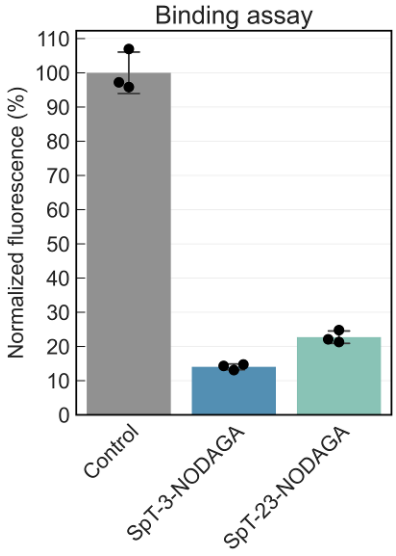

Fig. 13. ***Binding of SpT-NODAGA variants to the OMV surface.*** *The results of the binding test show that SpT-3-NODAGA inhibits SpT-CF binding significantly better than SpT-23-NODAGA.*

We evaluated both SpT-NODAGA variants for radiolabeling. The first radiolabeling approach (*Method 1*) resulted in 32.90% RCP and 43.17% RCP for SpT-3-NODAGA and SpT-23-NODAGA labeled OMVs respectively. (Fig. 14. A) Samples were then purified using a Sepharose CL-4B gravity column and the two fractions with the highest activity (0.9-1.3 ml elution volume) were pooled and analyzed with SEC-HPLC (Fig. 14. B, C). SEC-

HPLC analysis revealed only a single peak on the radio-chromatogram indicating 100% RCP (Fig. 14. D). This method resulted in an overall radiolabeling efficiency of 29.20% and 28.87% for SpT-3-NODAGA and SpT-23-NODAGA labeled OMVs respectively. After 3 hours, the RCP values for SpT-3-NODAGA and SpT-23-NODAGA labeled OMVs were determined to be 77.08% ± 0.24% and 81.61% ± 1.95%, respectively. Statistical analysis revealed a significant decrease in serum stability from 3 to 24 hours post-incubation amounting to a 0.51% decrease in RCP per hour (95% confidence interval: [0.43%, 0.58%]). Labeling with SpT-3-NODAGA also resulted in a significantly lower overall RCP compared to SpT-23-NODAGA during this time (71.86 ± 4.45% and 79.36 ± 3.96% respectively, $p = 0.0002$) (Fig. 14. E). In the second approach (*Method 2*) we labeled the peptides with ^{64}Cu first, then incubated the OMVs with the labeled peptides. The ^{64}Cu radiolabeling was successful for both peptides, resulting in ~95% RCP in both cases determined by RP-HPLC. Labeling OMVs with [^{64}Cu]SpT-3-NODAGA lead to a markedly higher RCP after 1h incubation (Welch's t-test $p = 0.05$) and significantly higher RCP at 2h and 4h incubation compared to [^{64}Cu]SpT-23-NODAGA (Welch's t-test $p < 0.01$) in line with our binding assay results (Fig. 14. F). Even after 4h incubation with the peptides, RCP was much lower than using *Method 1* (15.26% ± 0.21% for [^{64}Cu]SpT-3-NODAGA and 11.12% ± 0.12% for [^{64}Cu]SpT-23-NODAGA) (Fig. 14. G).

DOI:10.14753/SE.2024.3055

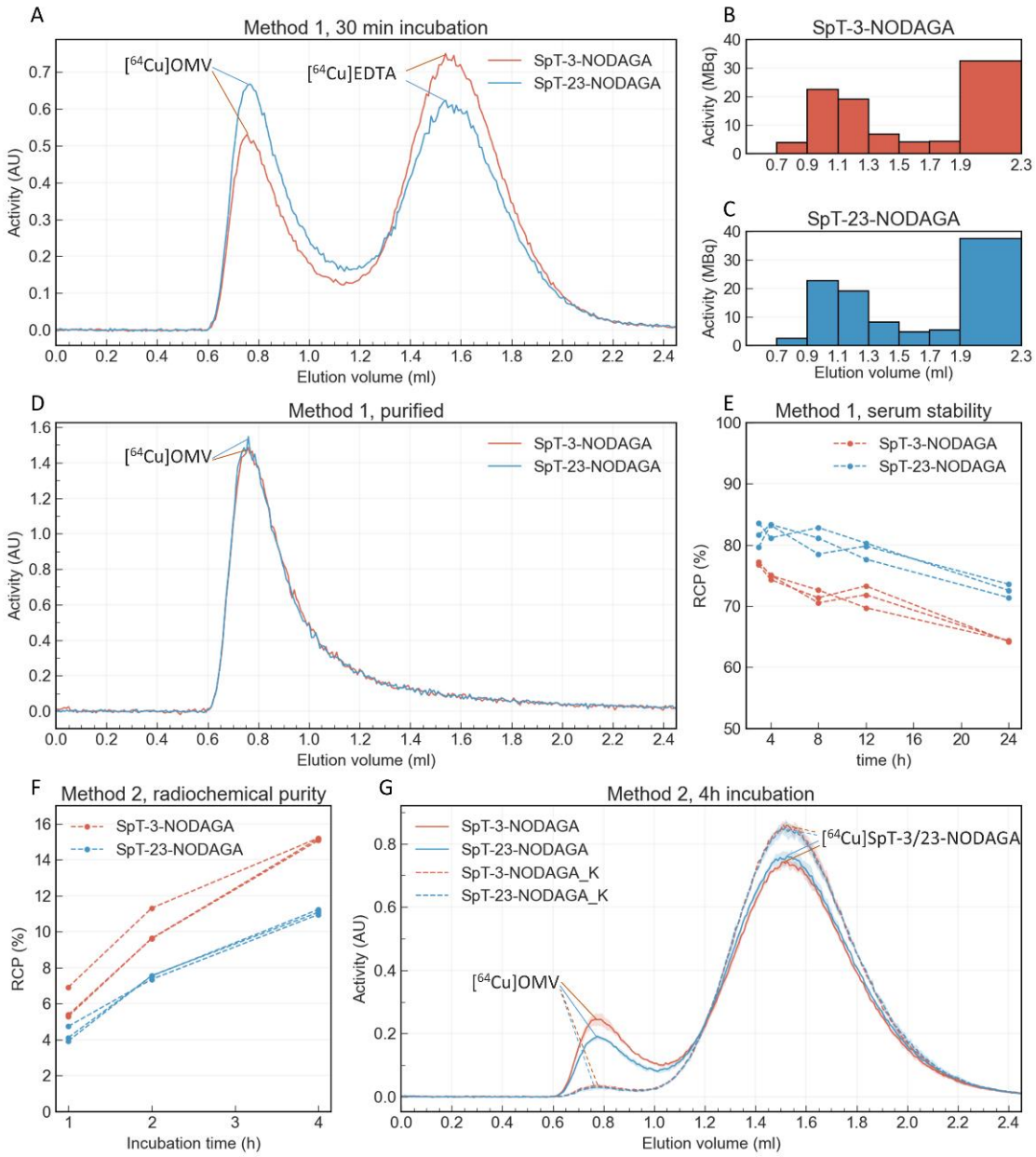

Fig. 14. ***OMV radiolabeling. A)*** *SEC-HPLC radiochromatogram of ^{64}Cu labeled pET28-ASpC OMVs prepared by Method 1. The first peak corresponds to ^{64}Cu bound to the OMVs, while the second peak corresponds to free ^{64}Cu chelated by EDTA.* ***B, C)*** *Radiochromatograms of ^{64}Cu-labeled OMVs (Method 1) obtained using a gravity column packed with Sepharose CL-4B.* ***D)*** *SEC-HPLC radiochromatogram following purification.* ***E)*** *In vitro serum stability analysis of ^{64}Cu-labeled OMVs (Method 1).* ***F)*** *pET28-ASpC*

OMVs were incubated with ^{64}Cu-labeled SpT-NODAGA variants and analyzed using SEC-HPLC (Method 2). ***G)*** *SEC-HPLC radiochromatogram showing the results of Method 2 after 4h incubation. SpT-3/23-NODAGA_K are negative controls. Curves represent the mean of multiple experiments, the shaded areas represent the standard deviation.*

4.1.4 In vivo imaging of OMV distribution

The biodistribution of radiolabeled OMVs and SpT-NODAGA variants in mice was measured using PET/MRI in three different time points (3h, 6h, 12h post injection). Decay-corrected standardized uptake values are reported in Table 1. Decay-corrected organ uptake in percentage of injected dose is reported in Table 2. The results are summarized in Fig. 15 and 16. In all time points, the uptake of liver and spleen was the highest for radiolabeled OMVs regardless of the SpT-NODAGA variant used. The radiolabeled peptides without OMVs showed a very different biodistribution pattern with the highest organ uptake measured in the kidneys, decreasing with time. This suggests that the peptides are eliminated mainly through renal clearance. For both OMVs and peptides, variable bladder activities were due to urination between measurements.

DOI:10.14753/SE.2024.3055

Table 1. Standardized Uptake Values (SUV) of different organs measured with PET/MRI.

		SUV (g/ml)			
		SpT-3-NODAGA	**SpT-23-NODAGA**	**SpT-3-OMV**	**SpT-23-OMV**
3h	**kidneys**	2.95	2.48	1.23	1.18
	liver	0.94	0.53	6.10	5.93
	heart	0.10	0.08	0.34	0.34
	brain	0.04	0.03	0.08	0.08
	lung	0.13	0.08	0.47	0.57
	spleen	0.10	0.14	6.89	6.01
	bladder	3.02	6.10	2.06	3.05
	intestines	0.32	0.40	0.54	0.49
6h	**kidneys**	2.42	2.18	1.15	1.23
	liver	1.02	0.36	5.02	4.92
	heart	0.12	0.08	0.42	0.38
	brain	0.05	0.03	0.08	0.09
	lung	0.13	0.09	0.68	0.63
	spleen	0.07	0.10	5.89	5.53
	bladder	1.60	1.03	0.99	0.87
	intestines	0.30	0.37	0.72	0.51
12h	**kidneys**	1.93	1.75	1.32	1.29
	liver	1.01	0.35	5.46	5.01
	heart	0.11	0.09	0.30	0.31
	brain	0.04	0.03	0.09	0.09
	lung	0.14	0.08	0.56	0.53
	spleen	0.09	0.11	5.65	5.00
	bladder	0.22	0.25	0.76	0.69
	intestines	0.29	0.24	0.78	0.56

DOI:10.14753/SE.2024.3055

Table 2. Injected dose (ID) percentages of different organs measured with PET/MRI.

		%ID			
		[^{64}Cu]SpT-3-NODAGA	**[^{64}Cu]SpT-23-NODAGA**	**[^{64}Cu]SpT-3-OMV**	**[^{64}Cu]SpT-23-OMV**
3h	**kidneys**	14.13%	9.65%	2.11%	1.83%
	liver	5.22%	2.38%	49.39%	47.46%
	heart	0.12%	0.10%	0.36%	0.36%
	brain	0.07%	0.06%	0.17%	0.17%
	lung	0.40%	0.33%	1.57%	1.85%
	spleen	0.06%	0.05%	7.37%	6.55%
	bladder	2.06%	4.24%	2.12%	2.10%
	intestines	4.54%	3.27%	4.91%	4.36%
6h	**kidneys**	11.66%	8.35%	2.08%	1.67%
	liver	6.10%	2.33%	46.82%	47.67%
	heart	0.15%	0.13%	0.44%	0.42%
	brain	0.09%	0.08%	0.16%	0.17%
	lung	0.40%	0.30%	1.17%	1.20%
	spleen	0.03%	0.05%	6.32%	6.38%
	bladder	1.25%	0.54%	0.64%	0.39%
	intestines	2.53%	3.50%	4.50%	4.31%
12h	**kidneys**	8.21%	6.38%	1.61%	1.87%
	liver	5.84%	1.82%	43.45%	45.58%
	heart	0.12%	0.12%	0.29%	0.36%
	brain	0.08%	0.09%	0.19%	0.17%
	lung	0.49%	0.27%	1.58%	1.26%
	spleen	0.04%	0.03%	5.46%	5.16%
	bladder	0.02%	0.02%	0.47%	0.14%
	intestines	2.99%	3.00%	6.37%	4.20%

DOI:10.14753/SE.2024.3055

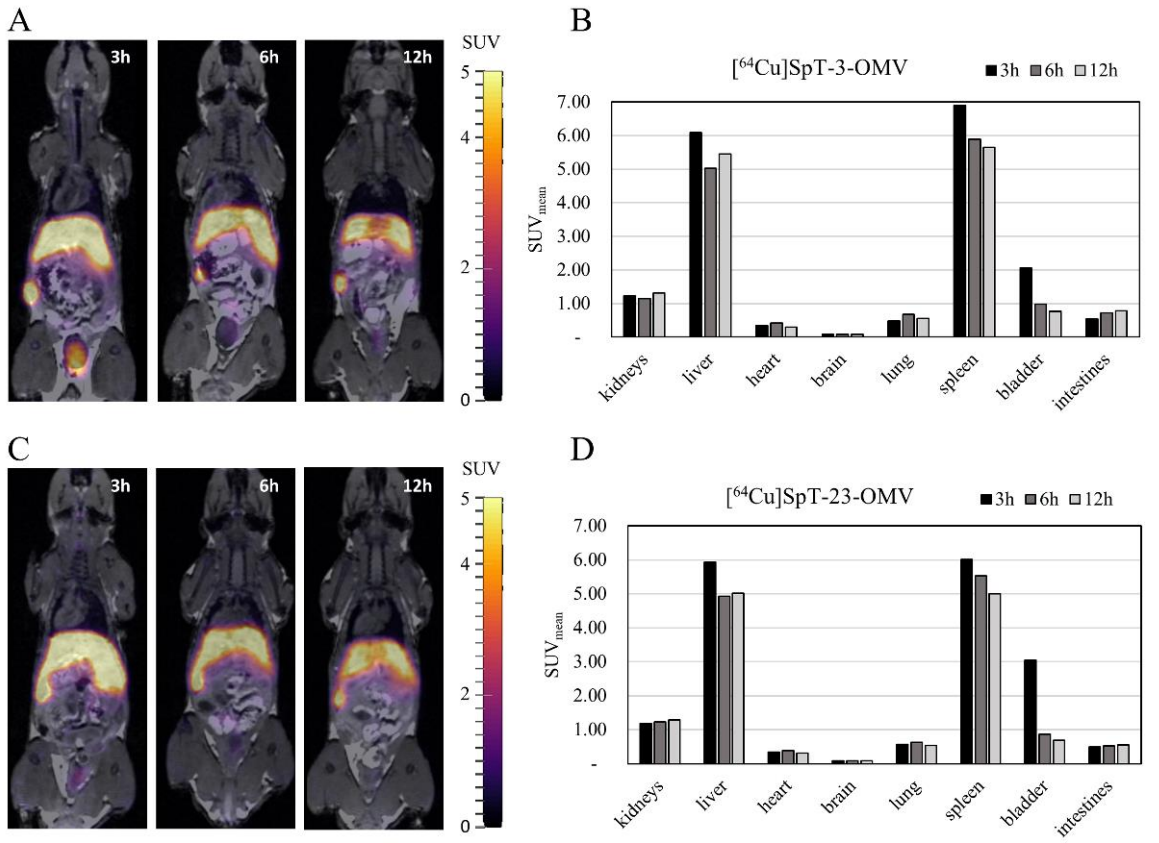

Fig. 15. ***In vivo biodistribution of radiolabeled OMVs. A)*** *Representative coronal slices of PET/MRI images taken 3, 6, and 12 hours after the injection of OMVs labeled using SpT-3-NODAGA.* ***B)*** *Decay-corrected* SUV_{mean} *of different organs of the same animal.* ***C)*** *Representative slices of PET/MRI images taken 3, 6, and 12 hours after the injection of OMVs labeled using SpT-23-NODAGA.* ***D)*** *Decay-corrected* SUV_{mean} *of different organs of the same animal.*

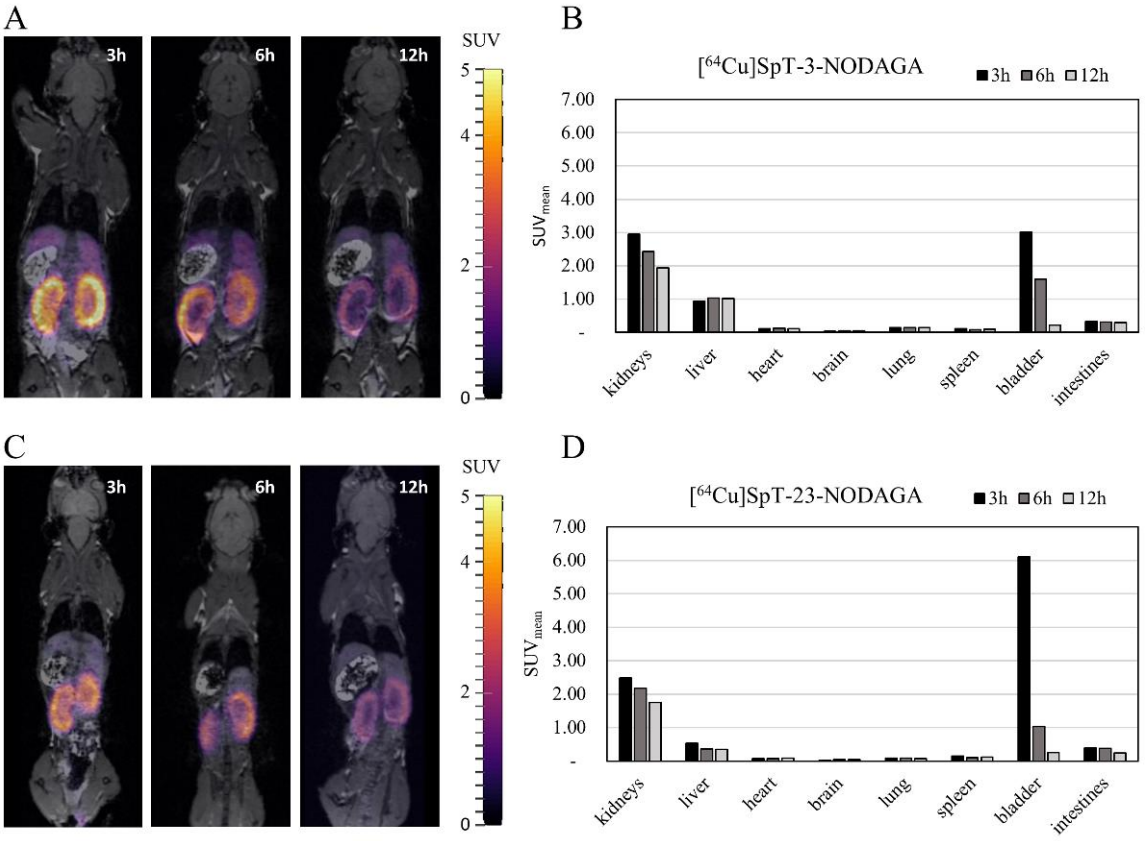

Fig. 16. ***In vivo biodistribution of radiolabeled SpT-3/23-NODAGA.*** ***A)*** *Representative slices of PET/MRI images taken 3, 6, and 12 hours after the injection of SpT-3-NODAGA labeled with ^{64}Cu.* ***B)*** *Decay-corrected SUV_{mean} of different organs of the same animal.* ***C)*** *Representative slices of PET/MRI images taken 3, 6, and 12 hours after the injection of SpT-23-NODAGA labeled with ^{64}Cu.* ***D)*** *Decay-corrected SUV_{mean} of different organs of the same animal.*

4.2 Systemic inflammation

[^{125}I]CLINME SPECT results obtained from SAE mice are shown in Fig. 17. Significantly elevated ($p = 0.05$) uptake was observed in the cerebrum ($4.23 \times 10^{-3} \pm 0.17 \times 10^{-3}$ ml^{-1} and $5.10 \times 10^{-3} \pm 0.49 \times 10^{-3}$ ml^{-1} for control and LPS treated respectively) and non-significant elevation in all other investigated brain areas.

DOI:10.14753/SE.2024.3055

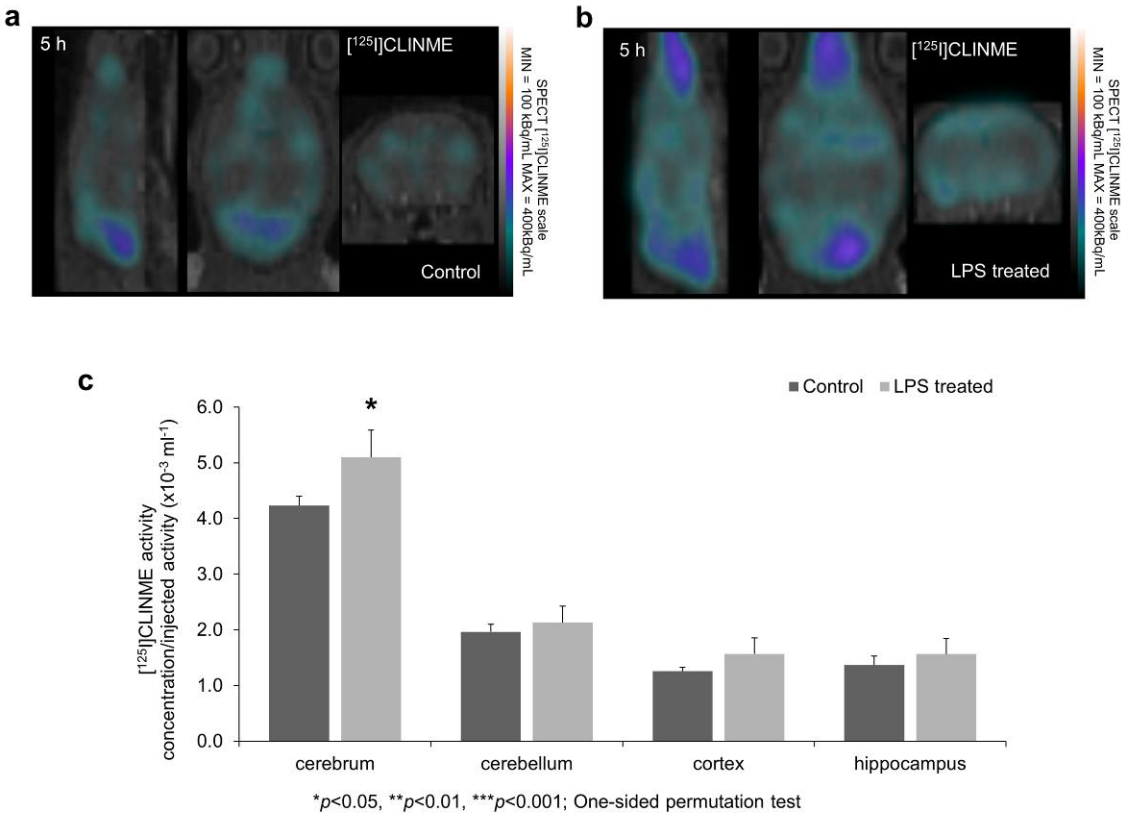

Fig. 17. ***Brain [^{125}I]CLINME uptake measured with SPECT.*** *SPECT coregistration with MRI showing [^{125}I]CLINME uptake changes after* ***A)*** *LPS-induced neuroinflammation compared to* ***B)*** *the control group. Arrows indicate example areas where the difference in radiotracer uptakes between the two groups is visually discernable.* ***C)*** *[^{125}I]CLINME uptake is significantly increased 5h after the LPS injection in the cerebrum (*p≤0.05 – One-sided permutation test).*

5. Discussion

5.1 Characteristics of BL21.V OMVs

Due to the high diversity of EVs and the multitude of research tools available, recommendations have been created by the International Society for Extracellular Vesicles

to standardize reporting and give researchers a useful guideline for their work. This guideline, titled “Minimal information for studies of extracellular vesicles” (or MISEV, for short) gives recommendations on the characterization, quantification and quality control of known and newly discovered EVs (97). Although the previous, 2018 edition did not cover prokaryotic vesicles, the updated 2023 edition includes them. In adherence to these guidelines, and to increase reproducibility, we determined the size distribution, morphology and IR spectrum of OMVs isolated from the novel *E. coli* BL21.V strain. We also used culture OD_{600} as a pre-isolation quality control measure, while SDS-PAGE and SEC-HPLC was used for post-isolation quality control. The OMV content of each isolate was determined using protein quantification. We report all of our methods in detail.

The size distribution of our vesicles measured using TEM is on the smaller side of previously reported OMV size ranges that typically fall within 10 nm to 300 nm (5, 98-102). However, size distributions from various sources are not always comparable and there is no standardized method to measure OMV size. Size measurements using different methods carried out on the same sample can give widely different results (103, 104) and each method has its limitations. For TEM measurements sample preparation and analysis could be possible sources of bias. EVs tend to collapse when applied to a TEM grid and there is no guarantee that vesicles of different sizes get adsorbed to the grid with the same likelihood. When size measurements are carried out manually on TEM images, the investigator has to make decisions as to which particles should be included based on their appearance on the photomicrographs. The inclusion criteria are unfortunately rarely reported. In this study, we included every round or slightly elliptic, clearly distinguishable particle with smooth borders in our size distribution measurements. This means that a number of micelles also might have been included as their features are very similar to OMVs on the photomicrographs.

IR spectroscopy is a fast, label-free method for studying molecular composition without perturbing the biological samples, so the characterization of intact OMVs is also possible. Unlike human blood-derived EVs, the fingerprint region of OMVs is dominated by strong bands between 1200 and 950 cm^{-1}, assigned to C-O-C vibrations. Besides phosphodiesters, peptidoglycans and lipopolysaccharides, common on the bacterial

membrane surface (affirmed by complex sugar vibrational bands at 1150, 1119, 1082, and 1036 cm^{-1}) might have a contribution to the enhanced intensity of this spectral region (105). The calculated P/L_{spectr} value is in line with our previous experiments on pure eukaryotic EVs (usually P/L_{spectr} falls between 0.5 and 2 (95, 106-108)) and has also been previously shown to be characteristic of EV quality (109, 110).

SDS-PAGE revealed a pattern similar to previously reported OMV isolates with characteristic OmpF bands (111-113). Unlike for many types of eukaryotic EVs, there are only a few specific markers of sample purity for some prokaryotic strains. In our experience, the relative intensity of the OmpF band on a PageBlue-stained gel photograph is a useful marker of OMV sample purity. This is most evident when comparing SDS-PAGE results before and after SEC purification (84).

Throughout this study, we quantified the vesicle content of purified OMV isolates based on protein content measured with a modified Lowry assay. Based on our previous experience (95), different protein quantification methods can give widely different results for the same EV samples. To investigate further, we have compared the Lowry assay with two other popular methods: the Bradford assay and the bicinchoninic acid assay (BCA) for OMV quantification (84). Our results suggested that although the protein contents determined by these methods can vary significantly, they are correlated and thus the choice of method has a small influence when comparing samples measured with the same method. However, care must be taken when comparing OMV protein contents determined using different methods.

5.2 Optimization of SpyCatcher surface display

To anchor SpyCather to the OMV surface, we genetically fused it to two different autotransporters. We compared four different plasmids including two with their originally published backbones (pAIDA-SpC with pAIDA1 backbone (59) and pHbpD-SpC with pHbpD(Δd1) backbone (6, 60-63)), and two with pET based backbones (pET28-ASpC and pET28-HSpC) to find the best one. The main points of comparison were surface display efficiency on bacteria, effect on OMV yield and OMV surface display of SpyCatcher. Both autotransporters are frequently used for bacterial surface display and pHbpD(Δd1) was even used previously to display SpyCatcher on the surface of OMVs (6, 59-63, 75, 114, 115). All plasmids are IPTG-inducible in *E. coli* BL21.V. All plasmids code the gene for lac repressor

(LacI). In the pET28-based plasmids, the transcription of AIDA-SpC and HbpD-SpC are under the control of the T7 promoter combined with a downstream lac operator. A T7 RNA polymerase, encoded in the genome of *E. coli* BL21.V under the control of a lacUV promoter can bind to this site and lead to much faster transcription compared to the wild type RNA polymerase of *E. coli* (116). In pAIDA-SpC, transcription is under the control pf a lacUV5 and lac operator, while in pHbpD-SpC, both a T7 promoter and a downstream lacUV5 promoter is present, both coupled by downstream lac operators.

To find the optimal induction protocol, we evaluated SpyCatcher surface display at different growth temperatures and IPTG concentrations. We have found that pAIDA-SpC leads to lower SpyCatcher expression on the bacterial surface compared to other plasmids in all inducing conditions. Our FCM results suggest that the main cause of the relatively poor performance of pAIDA-SpC was the plasmid backbone, most likely the low copy number and lack of T7 promoter, as cloning the *AIDA-SpyCatcher* gene into pET28 increased its expression to a level similar to pET28-HSpC.

A decrease in median expression and the appearance of different cell populations was observed for increasing IPTG concentrations in multiple conditions. These results are in line with the results of Zhang et al. (117), who found that the addition of IPTG can lead to the increase of non-producing cell populations ultimately leading to decreased membrane protein expression in *E. coli* BL21(DE3). This effect is more pronounced at 24 °C and in the case of pET28-based plasmids.

Cellular elongation was also observed in the case of Hbp-based plasmids. These morphological changes could be the result of the co-translational translocation of Hbp (118, 119) combined with its larger size and longer translation time, leading to Sec translocon blockage preventing other membrane proteins from being successfully expressed (120). Aggregation was also observed in the case of Hbp-based plasmids. The exact reason is unknown, however it is notable that HbpD-SpC has most of its original passenger domain present (except d1) (60) and although it has not been previously reported, it could be the case that high levels of Hbp surface expression can lead to autoaggregation similarly to other type Va autotransporters (121, 122). Based on our results a low IPTG concentration (40 μM) combined with a higher growth temperature of 37 °C could be used for optimal expression.

We decided to use SEC-HPLC to investigate whether the choice of surface display system could affect OMV yield. The main reason why the Lowry assay, which is the general OMV quantification method in our experiments was not used for this purpose is that it requires purified OMV samples to give reliable results, as any leftover proteins and peptides from the original culture medium would lead to significant bias when measuring crude samples. Using purified samples on the other hand could lead to significantly higher variability in the results due to errors introduced during purification. Using SEC-HPLC allowed us to determine the OMV quantity of samples without purification. A drawback of SEC-HPLC for EV quantification is that the UV absorbance signal of nano-sized vesicles is partially caused by scattering, thus it can be size-dependent. Therefore, it only has a limited usefulness for comparisons made between EVs harvested from different sources. Also, it is important to first demonstrate that the resin used for analysis can efficiently separate EVs from impurities in the sample. To prove that Sepharose CL-4B, the resin used in our experiments, is suitable we have previously analyzed OMV samples before and after SEC purification using SDS-PAGE, TEM and FTIR (84). SEC-HPLC results show a non-significant OMV yield decrease in the case of pHbpD-SpC, pET28-ASpC and pET28-HSpC, most prominently affecting pET28-ASpC. OMV yield being affected by autotransporter surface display has previously been reported in case constructs much larger than AIDA-SpC (63). The exact mechanism is unknown.

We further investigated which surface display system leads to the highest OMV SpyTag binding capacity. OMV SpT-CF binding at multiple time points was evaluated to find the necessary incubation time for saturation. We found that 24 hours was sufficient to reach saturation in all cases (84). Our results indicate that pET28-ASpC OMVs bind the most SpT-CF per vesicle. This is surprising given that FCM analysis did not reveal such differences. This could suggest that AIDA-SpC is selectively enriched in the OMV membrane. Similar preferential packing into OMVs has been demonstrated for many different compounds (38, 39, 123), including many autotransporters (124, 125). Based on these data, we decided to use pET28-ASpC for radiolabeling as the high levels of SpyCatcher on the OMV surface should lead to higher specific activity. The negative effect on OMV yield can be overcome by isolating larger quantities.

DOI:10.14753/SE.2024.3055

5.3 Radiolabeling of OMVs

To carry out the radiolabeling, we have synthetized two bifunctional chelators SpT-3-NODAGA and SpT-23-NODAGA. Both molecules are based on a SpyTag peptide extended downstream and upstream according to the original sequence of fibronectin-binding protein (64) labeled with the macrocyclic chelator NODAGA on either Lys^3 (SpT-3-NODAGA) or Lys^{23} (SpT-23-NODAGA). NODAGA was chosen because it can be labeled with ^{68}Ga and ^{64}Cu at mild reaction conditions with high specific activity and excellent stability (72, 126). We chose to include a chelator in two different positions to investigate whether the macrocycle could interfere with SpyCatcher-SpyTag binding via steric hindrance. We found that SpT-3-NODAGA could bind to OMVs with a significantly higher efficiency suggesting that C-terminal placement may lead to some amount of steric hindrance. This is also supported by our radiolabeling results with *Method 2*.

We tested two different approaches for ^{64}Cu radiolabeling. In *Method 1* we first decorated the OMVs with SpT-3/23-NODAGA, then continued with radiolabeling. In *Method 2* we first labeled SpT-3/23-NODAGA with ^{64}Cu and then carried on with the SpyCatcher-SpyTag reaction. Our results show that *Method 1* coupled with SEC purification is suitable for OMV radiolabeling but due to the slow kinetics of the reaction between OMV-bound SpyCatcher and [^{64}Cu]SpT-3/23-NODAGA *Method 2* is not feasible, as the slow increase of radiochemical purity during incubation has to compete with radioactive decay. We also experimented with ^{68}Ga labeling (data not shown), however, dynamic light scattering analysis revealed that the feasible pH range for the radiolabeling (pH ~3.6) caused the OMVs to precipitate during *Method 1,* and *Method 2* is too slow compared to the half-life of ^{68}Ga. Increasing the pH would have led to the formation of insoluble gallium-hydroxide products. We believe that *Method 2* could be significantly improved by using the SpyCatcher003/SpyTag003 system described by Keeble et al. (127)

It is important to note that EDTA was used to chelate free ^{64}Cu at the end of these reactions. In our experience, without the addition of EDTA ~100% of free ^{64}Cu binds to the OMVs aspecifically and although some of this radioactivity can be instantaneously removed by the addition of EDTA, an incubation of ~15 minutes is necessary to sufficiently remove aspecifically bound ^{64}Cu. However, even after longer incubations, some ^{64}Cu remains

associated with OMVs. We suspect that this fraction of ^{64}Cu is inside the OMV lumen and is slowly leaking out. The uptake of ^{64}Cu into the vesicles should be possible through OmpF (128). This could explain our serum stability results, where an RCP decrease of ~20% was visible in the first 3 hours likely corresponding to intraluminal ^{64}Cu followed by an additional ~0.51% decrease per hour for 21 hours corresponding to ^{64}Cu bound by NODAGA. These serum stability results indicate that after an early release of a small fraction of ^{64}Cu the labeled OMVs stay sufficiently stable for up to 24 hours.

5.4 In vivo imaging of OMV biodistribution

Using the radiolabeled OMVs we carried out PET/MRI measurements to assess the biodistribution of the OMVs. Preclinical PET is a non-invasive imaging method for the measurement of biodistribution data with high precision. Newer equipment generally reaches submillimeter spatial resolution and ~10% sensitivity (129). This method has multiple advantages over optical imaging often used for EV biodistribution studies (130). Although luminescence-based optical imaging has the advantage of enabling the investigation of biodistribution on a microscopic-cellular level, on the whole animal scale the light signal detected with these methods is subject to significant attenuation and scattering in the body imposing limitations on the experimental design. One such limitation is the choice of animal models used during the experiments. Using small rodents (mice) without fur (nude phenotype or removed before imaging) and investigating tissues/organs close to the surface can improve the quantifiability of these results. On the other hand, PET studies can be readily adapted to large animal models and can be translated to human medicine. The use of CT or MRI-based attenuation and scatter correction coupled with novel reconstruction methods make PET a quantitative imaging modality (131). Our results could be converted to give the amount of OMVs (expressed in mg/ml protein) in a given volume, however, due to the lack of a standardized OMV protein quantification method and the aforementioned variability of measured protein content we decided not to convert our biodistribution results.

This pattern of biodistribution observed (the liver and spleen having the highest uptake) is similar to previously reported OMV biodistribution data (44, 45), however, a fair comparison is hard to make due to the differences in administration routes, imaging time, and imaging modality. To assess the in vivo stability of our radiolabeling approach we also

carried out PET/MRI studies of [^{64}Cu]SpT-3-NODAGA and [^{64}Cu]SpT-23-NODAGA. Although the peptides showed fast renal clearance indicated by the high kidney and bladder activities and the low overall remaining activity in all other organs 3h post-injection, some unspecific binding was observed, mainly in the kidneys even 12h p.i. The large differences between the OMV and peptide distribution patterns, most notably the very low kidney uptake in the case of OMVs indicate that [^{64}Cu]SpT-3/23-NODAGA stays associated with the OMVs for at least 12 hours *in vivo*.

5.5 In vivo imaging in the SAE model

A significant increase in cerebral [^{125}I]CLINME uptake 5 following systemic LPS administration was observed. These results are in line with other TSPO tracers and mainly reflect the proliferation of microglia in the brain with smaller contributions from the increased TSPO expression of microglia and astrocytes and the TSPO receptors on invading peripheral macrophages (132). This suggests that radioidinated CLINME can be an important research tool to measure the neuroinflammatory manifestations of systemic inflammation.

6. Conclusions

In conclusion, our results provide new possibilities for the *in vivo* imaging of different aspects of host-microbiota interactions.

First of all, we have shown that the combination of a surface display system with a protein ligation system and a chelator enables specific and stable OMV radiolabeling suitable for molecular imaging. The modularity of our approach results in great versatility as these three main parts can be customized. Using our AIDA-SpC and NODAGA-based method as a template, various OMV-specific radiolabeling methods could be developed in the future to fit the specific requirements of the researcher. Our method could also be used as an "imaging module" for OMV based drug carrier and vaccine development, where bioengineered OMVs are often decorated with a protein ligation system into which the SpyCatcher-SpyTag-NODAGA system can be incorporated. Furthermore, our method could shed light on the distribution of OMVs originating from different bacterial strains residing in various body habitats and the change of this distribution in selected disease models.

Secondly, we have shown that radioiodinated CLINME can detect the early increase in cerebral TSPO binding sites associated with the neuroinflammatory changes present during sepsis. This proves the usefulness of a versatile radiotracer which can be used for both SPECT and PET imaging depending on the choice of iodine isotope. We believe this multi-modal property can be used for more flexible experimental design and promote a wider availability of TSPO imaging in translational research in the future.

Achievements:

1) A novel bacterial strain, *E. coli* BL21.V was designed.
2) The OMVs of *E. coli* BL21.V have been characterized.
3) The SpyCatcher-SpyTag protein ligation system combined with an autotransporter-based surface display system can be used for OMV radiolabeling.
4) [^{125}I]CLINME SPECT can be used to detect the early neuroinflammatory effects of systemic inflammation in mice.

DOI:10.14753/SE.2024.3055

7. Summary

In my thesis I focus on *in vivo* imaging methods that can be used to study host-microbe interactions.

We have designed a radiolabeling method that can be used to study the biodistribution of bacterial outer membrane vesicles *in vivo.* For our experiments, we created a novel bacterial strain, *E. coli* BL21.V with favorable properties for OMV production and bacterial surface display. Using this organism, we compared two different autotransporter-based surface display systems to anchor SpyCatcher on the OMV surface. Our results show that the AIDA-based system with a pET28 plasmid backbone leads to the highest number of available SpyTag binging sites on the OMV surface. Next, we developed synthetic bifunctional chelators based on SpyTag and the macrocyclic chelator NODAGA. Two SpyTag-NODAGA variants were compared (SpT-3-NODAGA and SpT-23-NODAGA). Our results indicate, that SpyTag-3-NODAGA can bind to SpyCatcher displayed on the OMV surface with higher efficiency. We have compared two ^{64}Cu radiolabeling methods by either first carrying out the SpyCatcher-SpyTag ligation followed by NODAGA ^{64}Cu chelation (*Method 1*) or first labeling SpT-NODAGA variants with ^{64}Cu followed by SpyCatcher-SpyTag ligation (*Method 2*). Our results show that *Method 1* can be used to prepare highly pure radiolabeled OMVs suitable for in vivo imaging. Our PET/MRI measurements show a similar OMV biodistribution in mice to previously reported data with the liver and spleen taking up most of the vesicles. Comparison with the biodistribution of labeled peptides and the results of an in vitro stability test indicate that most ^{64}Cu stays attached to OMVs during a 12 hour investigation period.

We also evaluated [^{125}I]CLINME SPECT for the early detection of neuroinflammation in a murine sepsis associated encephalopathy model. We have found that following the induction of systemic inflammation by LPS injection, [^{125}I]CLINME can be used to visualize the increase in cerebral TSPO binding sites associated with neuroinflammatory changes as early as 5 h.

8. References

1. Bertani B, Ruiz N. Function and Biogenesis of Lipopolysaccharides. EcoSal Plus. 2018;8(1).

2. Mazgaeen L, Gurung P. Recent Advances in Lipopolysaccharide Recognition Systems. Int J Mol Sci. 2020;21(2).

3. Tsuneyoshi N, Kohara J, Bahrun U, Saitoh S, Akashi S, Gauchat JF, et al. Penta-acylated lipopolisaccharide binds to murine MD-2 but does not induce the oligomerization of TLR4 required for signal transduction. Cell Immunol. 2006;244(1):57-64.

4. Kim SH, Kim KS, Lee SR, Kim E, Kim MS, Lee EY, et al. Structural modifications of outer membrane vesicles to refine them as vaccine delivery vehicles. Biochim Biophys Acta. 2009;1788(10):2150-9.

5. Gujrati V, Kim S, Kim SH, Min JJ, Choy HE, Kim SC, et al. Bioengineered bacterial outer membrane vesicles as cell-specific drug-delivery vehicles for cancer therapy. ACS Nano. 2014;8(2):1525-37.

6. van den Berg van Saparoea HB, Houben D, Kuijl C, Luirink J, Jong WSP. Combining Protein Ligation Systems to Expand the Functionality of Semi-Synthetic Outer Membrane Vesicle Nanoparticles. Front Microbiol. 2020;11:890.

7. Chaudhry N, Duggal AK. Sepsis Associated Encephalopathy. Adv Med. 2014;2014:762320.

8. Ning Q, Liu Z, Wang X, Zhang R, Zhang J, Yang M, et al. Neurodegenerative changes and neuroapoptosis induced by systemic lipopolysaccharide administration are reversed by dexmedetomidine treatment in mice. Neurol Res. 2017;39(4):357-66.

9. Laye S, Parnet P, Goujon E, Dantzer R. Peripheral administration of lipopolysaccharide induces the expression of cytokine transcripts in the brain and pituitary of mice. Brain Res Mol Brain Res. 1994;27(1):157-62.

10. Gabellec MM, Griffais R, Fillion G, Haour F. Expression of interleukin 1 alpha, interleukin 1 beta and interleukin 1 receptor antagonist mRNA in mouse brain: regulation by bacterial lipopolysaccharide (LPS) treatment. Brain Res Mol Brain Res. 1995;31(1-2):122-30.

11. Pitossi F, del Rey A, Kabiersch A, Besedovsky H. Induction of cytokine transcripts in the central nervous system and pituitary following peripheral administration of endotoxin to mice. J Neurosci Res. 1997;48(4):287-98.

12. Ban E, Haour F, Lenstra R. Brain interleukin 1 gene expression induced by peripheral lipopolysaccharide administration. Cytokine. 1992;4(1):48-54.

13. Qin L, Wu X, Block ML, Liu Y, Breese GR, Hong JS, et al. Systemic LPS causes chronic neuroinflammation and progressive neurodegeneration. Glia. 2007;55(5):453-62.

14. Hoogland IC, Houbolt C, van Westerloo DJ, van Gool WA, van de Beek D. Systemic inflammation and microglial activation: systematic review of animal experiments. J Neuroinflammation. 2015;12:114.

15. Ming Z, Wotton CA, Appleton RT, Ching JC, Loewen ME, Sawicki G, et al. Systemic lipopolysaccharide-mediated alteration of cortical neuromodulation involves increases in monoamine oxidase-A and acetylcholinesterase activity. J Neuroinflammation. 2015;12:37.

16. Abdel-Salam OM, Youness ER, Mohammed NA, Morsy SM, Omara EA, Sleem AA. Citric acid effects on brain and liver oxidative stress in lipopolysaccharide-treated mice. J Med Food. 2014;17(5):588-98.

17. Varatharaj A, Galea I. The blood-brain barrier in systemic inflammation. Brain Behav Immun. 2017;60:1-12.

18. Zhou H, Andonegui G, Wong CH, Kubes P. Role of endothelial TLR4 for neutrophil recruitment into central nervous system microvessels in systemic inflammation. J Immunol. 2009;183(8):5244-50.

19. Bohatschek M, Werner A, Raivich G. Systemic LPS injection leads to granulocyte influx into normal and injured brain: effects of ICAM-1 deficiency. Exp Neurol. 2001;172(1):137-52.

20. Szollosi D, Hegedus N, Veres DS, Futo I, Horvath I, Kovacs N, et al. Evaluation of Brain Nuclear Medicine Imaging Tracers in a Murine Model of Sepsis-Associated Encephalopathy. Mol Imaging Biol. 2018;20(6):952-62.

21. Wolf SA, Boddeke HW, Kettenmann H. Microglia in Physiology and Disease. Annu Rev Physiol. 2017;79:619-43.

22. Csaszar E, Lenart N, Cserep C, Kornyei Z, Fekete R, Posfai B, et al. Microglia modulate blood flow, neurovascular coupling, and hypoperfusion via purinergic actions. J Exp Med. 2022;219(3).

23. Ransohoff RM. A polarizing question: do M1 and M2 microglia exist? Nat Neurosci. 2016;19(8):987-91.

24. Banati RB, Middleton RJ, Chan R, Hatty CR, Kam WW, Quin C, et al. Positron emission tomography and functional characterization of a complete PBR/TSPO knockout. Nat Commun. 2014;5:5452.

25. Guilarte TR, Rodichkin AN, McGlothan JL, Acanda De La Rocha AM, Azzam DJ. Imaging neuroinflammation with TSPO: A new perspective on the cellular sources and subcellular localization. Pharmacol Ther. 2022;234:108048.

26. Kreisl WC, Kim MJ, Coughlin JM, Henter ID, Owen DR, Innis RB. PET imaging of neuroinflammation in neurological disorders. Lancet Neurol. 2020;19(11):940-50.

27. Nutma E, Fancy N, Weinert M, Tsartsalis S, Marzin MC, Muirhead RCJ, et al. Translocator protein is a marker of activated microglia in rodent models but not human neurodegenerative diseases. Nat Commun. 2023;14(1):5247.

28. Owen DR, Narayan N, Wells L, Healy L, Smyth E, Rabiner EA, et al. Pro-inflammatory activation of primary microglia and macrophages increases 18 kDa translocator protein expression in rodents but not humans. J Cereb Blood Flow Metab. 2017;37(8):2679-90.

29. Corica F, De Feo MS, Gorica J, Sidrak MMA, Conte M, Filippi L, et al. PET Imaging of Neuro-Inflammation with Tracers Targeting the Translocator Protein (TSPO), a Systematic Review: From Bench to Bedside. Diagnostics (Basel). 2023;13(6).

30. Boutin H, Chauveau F, Thominiaux C, Kuhnast B, Gregoire MC, Jan S, et al. In vivo imaging of brain lesions with [(11)C]CLINME, a new PET radioligand of peripheral benzodiazepine receptors. Glia. 2007;55(14):1459-68.

31. Mattner F, Quinlivan M, Greguric I, Pham T, Liu X, Jackson T, et al. Radiosynthesis, In Vivo Biological Evaluation, and Imaging of Brain Lesions with [123I]-CLINME, a New SPECT Tracer for the Translocator Protein. Dis Markers. 2015;2015:729698.

32. Sandiego CM, Gallezot JD, Pittman B, Nabulsi N, Lim K, Lin SF, et al. Imaging robust microglial activation after lipopolysaccharide administration in humans with PET. Proc Natl Acad Sci U S A. 2015;112(40):12468-73.

33. Hannestad J, Gallezot JD, Schafbauer T, Lim K, Kloczynski T, Morris ED, et al. Endotoxin-induced systemic inflammation activates microglia: [(1)(1)C]PBR28 positron emission tomography in nonhuman primates. Neuroimage. 2012;63(1):232-9.

34. Giridharan VV, Generoso JS, Lence L, Candiotto G, Streck E, Petronilho F, et al. A crosstalk between gut and brain in sepsis-induced cognitive decline. J Neuroinflammation. 2022;19(1):114.

35. Daniel N, Lecuyer E, Chassaing B. Host/microbiota interactions in health and diseases-Time for mucosal microbiology! Mucosal Immunol. 2021;14(5):1006-16.

36. Sun D, Chen P, Xi Y, Sheng J. From trash to treasure: the role of bacterial extracellular vesicles in gut health and disease. Front Immunol. 2023;14:1274295.

37. Avila-Calderon ED, Ruiz-Palma MDS, Aguilera-Arreola MG, Velazquez-Guadarrama N, Ruiz EA, Gomez-Lunar Z, et al. Outer Membrane Vesicles of Gram-Negative Bacteria: An Outlook on Biogenesis. Front Microbiol. 2021;12:557902.

38. Bonnington KE, Kuehn MJ. Protein selection and export via outer membrane vesicles. Biochim Biophys Acta. 2014;1843(8):1612-9.

39. Schwechheimer C, Kuehn MJ. Outer-membrane vesicles from Gram-negative bacteria: biogenesis and functions. Nat Rev Microbiol. 2015;13(10):605-19.

40. Caruana JC, Walper SA. Bacterial Membrane Vesicles as Mediators of Microbe - Microbe and Microbe - Host Community Interactions. Front Microbiol. 2020;11:432.

41. Gerritzen MJH, Martens DE, Wijffels RH, van der Pol L, Stork M. Bioengineering bacterial outer membrane vesicles as vaccine platform. Biotechnol Adv. 2017;35(5):565-74.

42. Chang-Monteagudo A, Ochoa-Azze R, Climent-Ruiz Y, Macias-Abraham C, Rodriguez-Noda L, Valenzuela-Silva C, et al. A single dose of SARS-CoV-2 FINLAY-FR-1A vaccine enhances neutralization response in COVID-19 convalescents, with a very good safety profile: An open-label phase 1 clinical trial. Lancet Reg Health Am. 2021;4:100079.

43. Kim OY, Dinh NT, Park HT, Choi SJ, Hong K, Gho YS. Bacterial protoplast-derived nanovesicles for tumor targeted delivery of chemotherapeutics. Biomaterials. 2017;113:68-79.

44. Jang SC, Kim SR, Yoon YJ, Park KS, Kim JH, Lee J, et al. In vivo kinetic biodistribution of nano-sized outer membrane vesicles derived from bacteria. Small. 2015;11(4):456-61.

45. Kim OY, Park HT, Dinh NTH, Choi SJ, Lee J, Kim JH, et al. Bacterial outer membrane vesicles suppress tumor by interferon-gamma-mediated antitumor response. Nat Commun. 2017;8(1):626.

46. Jones EJ, Booth C, Fonseca S, Parker A, Cross K, Miquel-Clopes A, et al. The Uptake, Trafficking, and Biodistribution of Bacteroides thetaiotaomicron Generated Outer Membrane Vesicles. Front Microbiol. 2020;11:57.

47. Huang Y, Beringhs AOR, Chen Q, Song D, Chen W, Lu X, et al. Genetically Engineered Bacterial Outer Membrane Vesicles with Expressed Nanoluciferase Reporter for in Vivo Bioluminescence Kinetic Modeling through Noninvasive Imaging. ACS Applied Bio Materials. 2019;2(12):5608-15.

48. Kuerban K, Gao X, Zhang H, Liu J, Dong M, Wu L, et al. Doxorubicin-loaded bacterial outer-membrane vesicles exert enhanced anti-tumor efficacy in non-small-cell lung cancer. Acta Pharm Sin B. 2020;10(8):1534-48.

49. Gujrati V, Prakash J, Malekzadeh-Najafabadi J, Stiel A, Klemm U, Mettenleiter G, et al. Bioengineered bacterial vesicles as biological nano-heaters for optoacoustic imaging. Nat Commun. 2019;10(1):1114.

50. Pastor Y, Larraneta E, Erhard A, Quincooces G, Penuelas I, Irache JM, et al. Dissolving Microneedles for Intradermal Vaccination against Shigellosis. Vaccines (Basel). 2019;7(4).

51. Siddiqui NA, Houson HA, Thomas SC, Blanco JR, O'Donnell RE, Hassett DJ, et al. Radiolabelled Bacterial Metallophores as Targeted PET Imaging Contrast Agents for Accurate Identification of Bacteria and Outer Membrane Vesicles in vivo. bioRxiv. 2020:2020.08.06.240119.

52. Li Z, Niu L, Wang L, Mei T, Shang W, Cheng X, et al. Biodistribution of (89)Zr-DFO-labeled avian pathogenic Escherichia coli outer membrane vesicles by PET imaging in chickens. Poult Sci. 2023;102(2):102364.

53. Khan AA, R TMdR. Radiolabelling of Extracellular Vesicles for PET and SPECT imaging. Nanotheranostics. 2021;5(3):256-74.

54. Fan E, Chauhan N, Udatha D, Leo JC, Linke D. Type V Secretion Systems in Bacteria. Microbiol Spectr. 2016;4(1).

55. Henderson IR, Navarro-Garcia F, Desvaux M, Fernandez RC, Ala'Aldeen D. Type V protein secretion pathway: the autotransporter story. Microbiol Mol Biol Rev. 2004;68(4):692-744.

56. Zude I, Leimbach A, Dobrindt U. Prevalence of autotransporters in Escherichia coli: what is the impact of phylogeny and pathotype? Int J Med Microbiol. 2014;304(3-4):243-56.

57. Jose J. Autodisplay: efficient bacterial surface display of recombinant proteins. Appl Microbiol Biotechnol. 2006;69(6):607-14.

58. Wilhelm S, Rosenau F, Kolmar H, Jaeger KE. Autotransporters with GDSL passenger domains: molecular physiology and biotechnological applications. Chembiochem. 2011;12(10):1476-85.

59. Jarmander J, Gustavsson M, Do TH, Samuelson P, Larsson G. A dual tag system for facilitated detection of surface expressed proteins in Escherichia coli. Microb Cell Fact. 2012;11:118.

60. van den Berg van Saparoea HB, Houben D, de Jonge MI, Jong WSP, Luirink J. Display of Recombinant Proteins on Bacterial Outer Membrane Vesicles by Using Protein Ligation. Appl Environ Microbiol. 2018;84(8).

61. Hjelm A, Soderstrom B, Vikstrom D, Jong WS, Luirink J, de Gier JW. Autotransporter-based antigen display in bacterial ghosts. Appl Environ Microbiol. 2015;81(2):726-35.

62. Jong WS, Daleke-Schermerhorn MH, Vikstrom D, Ten Hagen-Jongman CM, de Punder K, van der Wel NN, et al. An autotransporter display platform for the development of multivalent recombinant bacterial vector vaccines. Microb Cell Fact. 2014;13:162.

63. Daleke-Schermerhorn MH, Felix T, Soprova Z, Ten Hagen-Jongman CM, Vikstrom D, Majlessi L, et al. Decoration of outer membrane vesicles with multiple antigens by using an autotransporter approach. Appl Environ Microbiol. 2014;80(18):5854-65.

64. Zakeri B, Fierer JO, Celik E, Chittock EC, Schwarz-Linek U, Moy VT, et al. Peptide tag forming a rapid covalent bond to a protein, through engineering a bacterial adhesin. Proc Natl Acad Sci U S A. 2012;109(12):E690-7.

65. Salverda ML, Meinderts SM, Hamstra HJ, Wagemakers A, Hovius JW, van der Ark A, et al. Surface display of a borrelial lipoprotein on meningococcal outer membrane vesicles. Vaccine. 2016;34(8):1025-33.

66. Kim JY, Doody AM, Chen DJ, Cremona GH, Shuler ML, Putnam D, et al. Engineered bacterial outer membrane vesicles with enhanced functionality. J Mol Biol. 2008;380(1):51-66.

67. Zingl FG, Leitner DR, Thapa HB, Schild S. Outer membrane vesicles as versatile tools for therapeutic approaches. microLife. 2021;2.

68. Reddington SC, Howarth M. Secrets of a covalent interaction for biomaterials and biotechnology: SpyTag and SpyCatcher. Curr Opin Chem Biol. 2015;29:94-9.

69. Hatlem D, Trunk T, Linke D, Leo JC. Catching a SPY: Using the SpyCatcher-SpyTag and Related Systems for Labeling and Localizing Bacterial Proteins. Int J Mol Sci. 2019;20(9).

70. Gallus S, Peschke T, Paulsen M, Burgahn T, Niemeyer CM, Rabe KS. Surface Display of Complex Enzymes by in Situ SpyCatcher-SpyTag Interaction. Chembiochem. 2020;21(15):2126-31.

71. von Witting E, Garousi J, Lindbo S, Vorobyeva A, Altai M, Oroujeni M, et al. Selection of the optimal macrocyclic chelators for labeling with (111)In and (68)Ga improves contrast of HER2 imaging using engineered scaffold protein ADAPT6. Eur J Pharm Biopharm. 2019;140:109-20.

72. Ghosh SC, Pinkston KL, Robinson H, Harvey BR, Wilganowski N, Gore K, et al. Comparison of DOTA and NODAGA as chelators for (64)Cu-labeled immunoconjugates. Nucl Med Biol. 2015;42(2):177-83.

73. Pouresmaeil M, Azizi-Dargahlou S. Factors involved in heterologous expression of proteins in E. coli host. Arch Microbiol. 2023;205(5):212.

74. Rosano GL, Morales ES, Ceccarelli EA. New tools for recombinant protein production in Escherichia coli: A 5-year update. Protein Sci. 2019;28(8):1412-22.

75. Gustavsson M, Backlund E, Larsson G. Optimisation of surface expression using the AIDA autotransporter. Microb Cell Fact. 2011;10:72.

76. Premjani V, Tilley D, Gruenheid S, Le Moual H, Samis JA. Enterohemorrhagic Escherichia coli OmpT regulates outer membrane vesicle biogenesis. FEMS Microbiol Lett. 2014;355(2):185-92.

77. Schwechheimer C, Rodriguez DL, Kuehn MJ. NlpI-mediated modulation of outer membrane vesicle production through peptidoglycan dynamics in Escherichia coli. Microbiologyopen. 2015;4(3):375-89.

78. Park KS, Choi KH, Kim YS, Hong BS, Kim OY, Kim JH, et al. Outer membrane vesicles derived from Escherichia coli induce systemic inflammatory response syndrome. PLoS One. 2010;5(6):e11334.

79. Shah B, Sullivan CJ, Lonergan NE, Stanley S, Soult MC, Britt LD. Circulating bacterial membrane vesicles cause sepsis in rats. Shock. 2012;37(6):621-8.

80. Mamat U, Wilke K, Bramhill D, Schromm AB, Lindner B, Kohl TA, et al. Detoxifying Escherichia coli for endotoxin-free production of recombinant proteins. Microb Cell Fact. 2015;14:57.

81. Jensen SI, Nielsen AT. Multiplex Genome Editing in Escherichia coli. Methods Mol Biol. 2018;1671:119-29.

82. Jensen SI, Lennen RM, Herrgard MJ, Nielsen AT. Seven gene deletions in seven days: Fast generation of Escherichia coli strains tolerant to acetate and osmotic stress. Sci Rep. 2015;5:17874.

83. Baba T, Ara T, Hasegawa M, Takai Y, Okumura Y, Baba M, et al. Construction of Escherichia coli K-12 in-frame, single-gene knockout mutants: the Keio collection. Mol Syst Biol. 2006;2:2006 0008.

84. Szollosi D, Hajdrik P, Tordai H, Horvath I, Veres DS, Gillich B, et al. Molecular imaging of bacterial outer membrane vesicles based on bacterial surface display. Sci Rep. 2023;13(1):18752.

85. Nikitas P, Pappa-Louisi A, Papageorgiou A. On the equations describing chromatographic peaks and the problem of the deconvolution of overlapped peaks. J Chromatogr A. 2001;912(1):13-29.

86. McKinney W, editor Data Structures for Statistical Computing in Python2010.

87. Waskom ML. seaborn: statistical data visualization. Journal of Open Source Software. 2021;6(60):3021.

88. Hunter JD. Matplotlib: A 2D Graphics Environment. Computing in Science & Engineering. 2007;9(3):90-5.

89. Fedorov A, Beichel R, Kalpathy-Cramer J, Finet J, Fillion-Robin JC, Pujol S, et al. 3D Slicer as an image computing platform for the Quantitative Imaging Network. Magn Reson Imaging. 2012;30(9):1323-41.

90. Virtanen P, Gommers R, Oliphant TE, Haberland M, Reddy T, Cournapeau D, et al. SciPy 1.0: fundamental algorithms for scientific computing in Python. Nature Methods. 2020;17(3):261-72.

91. Team RC. R: A Language and Environment for Statistical Computing. 2021.

92. Pinheiro J, Bates D, Team RC. nlme: Linear and Nonlinear Mixed Effects Models. 2022.

93. Qing G, Gong N, Chen X, Chen J, Zhang H, Wang Y, et al. Natural and engineered bacterial outer membrane vesicles. Biophysics Reports. 2019;5(4):184-98.

94. David L, Taieb F, Penary M, Bordignon PJ, Planes R, Bagayoko S, et al. Outer membrane vesicles produced by pathogenic strains of Escherichia coli block autophagic flux and exacerbate inflammasome activation. Autophagy. 2022;18(12):2913-25.

95. Szentirmai V, Wacha A, Nemeth C, Kitka D, Racz A, Heberger K, et al. Reagent-free total protein quantification of intact extracellular vesicles by attenuated total reflection Fourier transform infrared (ATR-FTIR) spectroscopy. Anal Bioanal Chem. 2020;412(19):4619-28.

96. Maurer J, Jose J, Meyer TF. Characterization of the essential transport function of the AIDA-I autotransporter and evidence supporting structural predictions. J Bacteriol. 1999;181(22):7014-20.

97. Welsh JA, Goberdhan DCI, O'Driscoll L, Buzas EI, Blenkiron C, Bussolati B, et al. Minimal information for studies of extracellular vesicles (MISEV2023): From basic to advanced approaches. J Extracell Vesicles. 2024;13(2):e12404.

98. Fantappie L, de Santis M, Chiarot E, Carboni F, Bensi G, Jousson O, et al. Antibody-mediated immunity induced by engineered Escherichia coli OMVs carrying heterologous antigens in their lumen. J Extracell Vesicles. 2014;3.

99. Kosgodage US, Matewele P, Mastroianni G, Kraev I, Brotherton D, Awamaria B, et al. Peptidylarginine Deiminase Inhibitors Reduce Bacterial Membrane Vesicle Release and Sensitize Bacteria to Antibiotic Treatment. Front Cell Infect Microbiol. 2019;9:227.

100. Kulkarni HM, Nagaraj R, Jagannadham MV. Protective role of E. coli outer membrane vesicles against antibiotics. Microbiol Res. 2015;181:1-7.

101. Svennerholm K, Park KS, Wikstrom J, Lasser C, Crescitelli R, Shelke GV, et al. Escherichia coli outer membrane vesicles can contribute to sepsis induced cardiac dysfunction. Sci Rep. 2017;7(1):17434.

102. Kim SW, Park SB, Im SP, Lee JS, Jung JW, Gong TW, et al. Outer membrane vesicles from beta-lactam-resistant Escherichia coli enable the survival of beta-lactam-susceptible E. coli in the presence of beta-lactam antibiotics. Sci Rep. 2018;8(1):5402.

103. Chernyshev VS, Rachamadugu R, Tseng YH, Belnap DM, Jia Y, Branch KJ, et al. Size and shape characterization of hydrated and desiccated exosomes. Anal Bioanal Chem. 2015;407(12):3285-301.

104. van der Pol E, Coumans FA, Grootemaat AE, Gardiner C, Sargent IL, Harrison P, et al. Particle size distribution of exosomes and microvesicles determined by transmission electron microscopy, flow cytometry, nanoparticle tracking analysis, and resistive pulse sensing. J Thromb Haemost. 2014;12(7):1182-92.

105. Kochan K, Perez-Guaita D, Pissang J, Jiang JH, Peleg AY, McNaughton D, et al. In vivo atomic force microscopy-infrared spectroscopy of bacteria. J R Soc Interface. 2018;15(140).

106. Kitka D, Mihaly J, Fraikin JL, Beke-Somfai T, Varga Z. Detection and phenotyping of extracellular vesicles by size exclusion chromatography coupled with on-line fluorescence detection. Sci Rep. 2019;9(1):19868.

107. Romanszki L, Varga Z, Mihaly J, Keresztes Z, Thompson M. Electromagnetic Piezoelectric Acoustic Sensor Detection of Extracellular Vesicles through Interaction with Detached Vesicle Proteins. Biosensors (Basel). 2020;10(11).

108. Szigyarto IC, Deak R, Mihaly J, Rocha S, Zsila F, Varga Z, et al. Flow Alignment of Extracellular Vesicles: Structure and Orientation of Membrane-Associated Bio-macromolecules Studied with Polarized Light. Chembiochem. 2018;19(6):545-51.

109. Mihaly J, Deak R, Szigyarto IC, Bota A, Beke-Somfai T, Varga Z. Characterization of extracellular vesicles by IR spectroscopy: Fast and simple classification based on amide and CH stretching vibrations. Biochim Biophys Acta Biomembr. 2017;1859(3):459-66.

110. Thery C, Witwer KW, Aikawa E, Alcaraz MJ, Anderson JD, Andriantsitohaina R, et al. Minimal information for studies of extracellular vesicles 2018 (MISEV2018): a position statement of the International Society for Extracellular Vesicles and update of the MISEV2014 guidelines. J Extracell Vesicles. 2018;7(1):1535750.

111. Chutkan H, Macdonald I, Manning A, Kuehn MJ. Quantitative and qualitative preparations of bacterial outer membrane vesicles. Methods Mol Biol. 2013;966:259-72.

112. Lee EY, Choi DS, Kim KP, Gho YS. Proteomics in gram-negative bacterial outer membrane vesicles. Mass Spectrom Rev. 2008;27(6):535-55.

113. Lee EY, Bang JY, Park GW, Choi DS, Kang JS, Kim HJ, et al. Global proteomic profiling of native outer membrane vesicles derived from Escherichia coli. Proteomics. 2007;7(17):3143-53.

114. Jiang L, Driedonks TAP, Jong WSP, Dhakal S, van den Berg van Saparoea HB, Sitaras I, et al. A bacterial extracellular vesicle-based intranasal vaccine against SARS-CoV-2 protects against disease and elicits neutralizing antibodies to wild-type and Delta variants. bioRxiv. 2022.

115. Fathi-Roudsari M, Behmanesh M, Salmanian AH, Sadeghizadeh M, Khajeh K. Functional Surface Display of Laccase in a Phenol-Inducible Bacterial Circuit for Bioremediation Purposes. Iran Biomed J. 2018;22(3):202-9.

116. Wagner S, Klepsch MM, Schlegel S, Appel A, Draheim R, Tarry M, et al. Tuning Escherichia coli for membrane protein overexpression. Proc Natl Acad Sci U S A. 2008;105(38):14371-6.

117. Zhang Z, Kuipers G, Niemiec L, Baumgarten T, Slotboom DJ, de Gier JW, et al. High-level production of membrane proteins in E. coli BL21(DE3) by omitting the inducer IPTG. Microb Cell Fact. 2015;14:142.

118. Sijbrandi R, Urbanus ML, ten Hagen-Jongman CM, Bernstein HD, Oudega B, Otto BR, et al. Signal recognition particle (SRP)-mediated targeting and Sec-dependent translocation of an extracellular Escherichia coli protein. J Biol Chem. 2003;278(7):4654-9.

119. Hornstrom D, Larsson G, van Maris AJA, Gustavsson M. Molecular optimization of autotransporter-based tyrosinase surface display. Biochim Biophys Acta Biomembr. 2019;1861(2):486-94.

120. Wagner S, Baars L, Ytterberg AJ, Klussmeier A, Wagner CS, Nord O, et al. Consequences of membrane protein overexpression in Escherichia coli. Mol Cell Proteomics. 2007;6(9):1527-50.

121. Trunk T, Khalil HS, Leo JC. Bacterial autoaggregation. AIMS Microbiol. 2018;4(1):140-64.

122. Nwoko EQA, Okeke IN. Bacteria autoaggregation: how and why bacteria stick together. Biochem Soc Trans. 2021;49(3):1147-57.

123. Haurat MF, Aduse-Opoku J, Rangarajan M, Dorobantu L, Gray MR, Curtis MA, et al. Selective sorting of cargo proteins into bacterial membrane vesicles. J Biol Chem. 2011;286(2):1269-76.

124. Lappann M, Otto A, Becher D, Vogel U. Comparative proteome analysis of spontaneous outer membrane vesicles and purified outer membranes of Neisseria meningitidis. J Bacteriol. 2013;195(19):4425-35.

125. Liu J, Hsieh CL, Gelincik O, Devolder B, Sei S, Zhang S, et al. Proteomic characterization of outer membrane vesicles from gut mucosa-derived fusobacterium nucleatum. J Proteomics. 2019;195:125-37.

126. Pohle K, Notni J, Bussemer J, Kessler H, Schwaiger M, Beer AJ. 68Ga-NODAGA-RGD is a suitable substitute for (18)F-Galacto-RGD and can be produced with high specific activity in a cGMP/GRP compliant automated process. Nucl Med Biol. 2012;39(6):777-84.

127. Keeble AH, Turkki P, Stokes S, Khairil Anuar INA, Rahikainen R, Hytonen VP, et al. Approaching infinite affinity through engineering of peptide-protein interaction. Proc Natl Acad Sci U S A. 2019.

128. Andrei A, Ozturk Y, Khalfaoui-Hassani B, Rauch J, Marckmann D, Trasnea PI, et al. Cu Homeostasis in Bacteria: The Ins and Outs. Membranes (Basel). 2020;10(9).

129. Amirrashedi M, Zaidi H, Ay MR. Advances in Preclinical PET Instrumentation. PET Clin. 2020;15(4):403-26.

130. Cunha L, Szigeti K, Mathe D, Metello LF. The role of molecular imaging in modern drug development. Drug Discov Today. 2014;19(7):936-48.

131. Kuntner C, Stout D. Quantitative preclinical PET imaging: opportunities and challenges. 2014;2.

132. Van Camp N, Lavisse S, Roost P, Gubinelli F, Hillmer A, Boutin H. TSPO imaging in animal models of brain diseases. Eur J Nucl Med Mol Imaging. 2021;49(1):77-109.

9. Bibliography

Publications related to the thesis

1. Szöllősi D, Hegedűs N, Veres D, Futo I, Horvath I, Stelczerné Kovács N, et al. Evaluation of Brain Nuclear Medicine Imaging Tracers in a Murine Model of Sepsis-Associated Encephalopathy. Mol Imaging Biol. 2018;20(6):952-62.
2. Szöllősi D, Hajdrik P, Tordai H, Horváth I, Veres D, Gillich B, et al. Molecular imaging of bacterial outer membrane vesicles based on bacterial surface display. Sci Rep. 2023;13(1).

Publications not related to the thesis

1. Tóth L, Szöllősi D, Kis-Petik K, Oszwald E, Kálmán M. Early phenomena following cryogenic lesions of rat brain - a preliminary study. Acta Biol Szeged. 2015;59:361-9.
2. Kálmán M, Tóth L, Szöllősi D, Oszwald E, Mahalek J, Sadeghian S. Correlation between extravasation and alterations of cerebrovascular laminin and β-dystroglycan immunoreactivity following cryogenic lesions in rats. J Neuropath Exp Neur. 2017;76(11):929-41.
3. Szöllősi D, Toth L, Kálmán M. Postmortem immunohistochemical alterations following cerebral lesions: A possible pathohistological importance of the beta-dystroglycan immunoreactivity. Neuropathology. 2018;38(3):207-17.
4. Szigeti K, Hegedűs N, Rácz K, Horváth I, Veres D, Szöllősi D, et al. Thallium Labeled Citrate-Coated Prussian Blue Nanoparticles as Potential Imaging Agent. Contrast Media Mol Imaging. 2018;2018.
5. Tóth L, Szöllősi D, Kis-Petik K, Adorján I, Erdélyi F, Kálmán M. The First Postlesion Minutes: An In Vivo Study of Extravasation and Perivascular Astrocytes Following Cerebral Lesions in Various Experimental Mouse Models. J Histochem Cytochem. 2019;67(1):29-39.
6. David T, Hlinova V, Kubicek V, Bergmann R, Striese F, Berndt N, et al. Improved Conjugation, 64-Cu Radiolabeling, in Vivo Stability, and Imaging Using

Nonprotected Bifunctional Macrocyclic Ligands: Bis(Phosphinate) Cyclam (BPC) Chelators. J Med Chem. 2018;61(19):8774-96.

7. Óriás IV, Gyánó M, Góg I, Szöllősi D, Veres D, Nagy Z, et al. Digital Variance Angiography as a Paradigm Shift in Carbon Dioxide Angiography. Invest Radiol. 2019;54(7):428-36.
8. Keszthelyi S, Szöllősi D, Strobel L, Osváth S, Szigeti K, Pónya Z, et al. Novel, X‐ray supported kinetic imaging of hidden‐lifestyle arthropods. Insect Sci. 2021;28(1):281-4.
9. Gaál A, Garay T, Horváth I, Máthé D, Szöllősi D, Veres D, et al. Development and In Vivo Application of a Water-Soluble Anticancer Copper Ionophore System Using a Temperature-Sensitive Liposome Formulation. Pharmaceutics. 2020;12(5).
10. Bastian MB, Konig AM, Viniol S, Gyánó M, Szöllősi D, Góg I, et al. Digital Variance Angiography in Lower-Limb Angiographywith Metal Implants. Cardiovasc Inter Rad. 2021;44(3):452-9.
11. Óriás IV, Szöllősi D, Gyánó M, Veres D, Nardai S, Csobay-Novák C, et al. Initial evidence of a 50% reduction of contrast media using digital variance angiography in endovascular carotid interventions. Eur J Radiol Open. 2020;7.
12. Ritter Z, Zámbó K, Jia X, Szöllősi D, Dezső D, Alizadeh H, et al. Intraperitoneal glucose transport to micrometastasis: A multimodal in vivo imaging investigation in a mouse lymphoma model. Int J Mol Sci. 2021;22(9).
13. Gyánó M, Berczeli M, Csobay-Novák C, Szöllősi D, Óriás IV, Góg I, et al. Digital variance angiography allows about 70% decrease of DSA-related radiation exposure in lower limb X-ray angiography. Sci Rep. 2021;11(1).
14. Thomas RP, Bastian MB, Viniol S, König AM, Amin SS, Eldergash O, et al. Digital Variance Angiography in Selective Lower Limb Interventions. J Vasc Interv Radiol. 2022;33(2):104-12.
15. Ritter Z, Zámbó K, Balogh P, Szöllősi D, Jia X, Balázs Á, et al. In situ lymphoma imaging in a spontaneous mouse model using the Cerenkov Luminescence of F-18 and Ga-67 isotopes. Sci Rep. 2021;11(1).

16. Juriga D, Kálmán EÉ, Juriga-Tóth K, Barczikai D, Szöllősi D, Földes A, et al. Analysis of Three-Dimensional Cell Migration in Dopamine-Modified Poly(aspartic acid)-Based Hydrogels. Gels-Basel. 2022;8(2).
17. Császár E, Lénárt N, Cserép C, Környei Z, Fekete R, Pósfai B, et al. Microglia modulate blood flow, neurovascular coupling, and hypoperfusion via purinergic actions. J Exp Med. 2022;219(3).
18. Arndt C, Bergmann RK, Striese F, Merkel KG, Máthé D, Loureiro LR, et al. Development and Functional Characterization of a Versatile Radio-/Immunotheranostic Tool for Prostate Cancer Management. Cancers. 2022;14(8).
19. Merkel KG, Szöllősi D, Horváth I, Jezsó B, Baranyai Z, Szigeti K, et al. Radiolabeling of Platelets with 99mTc-HYNIC-Duramycin for In Vivo Imaging Studies. Int J Mol Sci. 2023;24(23).

DOI:10.14753/SE.2024.3055

10. Acknowledgements

I would like to thank my supervisor, Krisztián Szigeti for his continuous support during my doctoral studies. His patience and optimism created an environment in the *in vivo* imaging workgroup where everyone could express and implement their best ideas. I also express my gratitude to Domokos Máthé for his guidance and introducing me to ideas and ways of thinking that helped me better understand science in general, and its place in the world. I would also like to thank Zoltán Varga for his invaluable support during our experiments. Our work together inspired me to study extracellular vesicles and without his help, I wouldn't have been able to learn the basics of radiochemistry, two of the main topics of my dissertation. I would also like to thank Dániel Veres for teaching me how to analyze experimental results and his continuous help with statistics. Furthermore, I am thankful for the support of Hedvig Tordai, who taught me almost everything I know about molecular biology, which played an essential role in the success of my research. I am grateful for the help of Ralf Bergmann, whose ideas and expertise in small animal imaging greatly helped our research. I would like to thank Szilvia Bősze and Ildikó Szabó for making our ideas into reality with their expertise in organic chemistry. I am grateful to Judith Mihály and László Smeller for their help with spectroscopy. I would also like to thank my friend Balázs Barátki, and Dorottya Kövesdi for helping us with the flow cytometry experiments. Furthermore, I thank Polett Hajdrik, Anikó Gaál, Ildikó Horváth, Krisztina Lór, Bernadett Gillich and Bálint Jézsó for their help in many of our experiments. I am grateful for the help Wouter Jong and Bart van den Berg van Saparoea who gifted me the plasmid on which nearly half of our experiments were based.

I would also like to thank the Head of Department, Miklós Kellermayer for supporting our project. Without his support, most of our experiments would not have been possible. I feel grateful for working at the Department of Biophysics and Radiation Biology and being able to meet the many wonderful people there, whose thought-provoking ideas I've always loved to hear.

Last, but certainly not least, I would like to thank my family, who supported me throughout the ups and downs of my doctoral years with patience and understanding.